Computer Methods in Applied Mechanics and Engineering 452 (2026) 118690

Contents lists available at ScienceDirect

Comput. Methods Appl. Mech. Engrg.

journal homepage: www.elsevier.com/locate/cma

Generating high-fidelity microstructures of polycrystalline materials with prescribed higher-order texture tensors

Maximilian Krause [a], Thomas Böhlke [b], Matti Schneider [a,c,d,*]

[a] University of Duisburg-Essen, Institute of Engineering Mathematics, Germany
[b] Karlsruhe Institute of Technology, Institute of Engineering Mechanics, Germany
[c] Fraunhofer Institute for Industrial Mathematics ITWM, Kaiserslautern, Germany
[d] CENIDE Center for Nanointegration, University of Duisburg-Essen, Germany

ARTICLE INFO

Keywords:
Microstructure generation
Polycrystals
Texture coefficients
Stochastic homogenization
Yield function
Moment-matching

ABSTRACT

We introduce an efficient computational procedure for generating polycrystalline microstructures which permits studying the influence of specific texture-tensor orders on the resulting effective mechanical response, both in the linear elastic and the inelastic case. The crystallographic texture of a polycrystalline material is described by the Orientation Distribution Function (ODF). For practical computations, only the Fourier coefficients – called texture coefficients – of the ODF up to a certain order are of interest. In the work at hand, we wish to investigate this microstructure-property relationship. We interpret the task of approximating the texture coefficients of a microstructure realization as a *moment-matching*, i.e., quadrature, problem, and introduce efficient techniques for generating finite sets of orientations which exactly conform to prescribed polynomial texture terms. First, the microstructure morphology is generated via a well-established Laguerre-tessellation-based approach. Subsequently, the crystal grains are assigned a finite set of orientations which realize prescribed texture coefficients. We exploit the sparse representation of the action of the rotation group $SO(3)$ on higher-order tensors to reduce the computational expense from exponential to cubic in the tensor order.

We consider polycrystalline copper as an example material and study the influence of texture terms of different polynomial order on the effective elastic properties and the anisotropy of initial yielding. For a large ensemble of polycrystal microstructures, we find that the elastic properties are mainly influenced by terms up to fourth order, whereas characterizing the yield function accurately requires higher-order texture terms.

To encourage further study of the texture dependence of nonlinear material properties, we provide an open-source python implementation of our algorithm.

1. Introduction

1.1. State of the art

Computational homogenization uses simulations to obtain the macroscopic behavior of heterogeneous materials based on an explicit resolution of the underlying microstructure. Microstructures which arise from stochastic processes are modeled as stochastic ensembles [1]. Computational homogenization operates on volume elements, i.e., realizations of the ensemble on cells of finite

* Corresponding author.
E-mail address: matti.schneider@uni-due.de (M. Schneider).

https://doi.org/10.1016/j.cma.2025.118690
Received 22 July 2025; Received in revised form 22 November 2025; Accepted 18 December 2025
Available online 8 January 2026

volume [2,3]. Due to the finite volume and the randomness of the realization, the expected statistics of the ensemble are only *approximated* on the considered volume. Moreover, there are infinitely many possible statistics, and only finitely many can be considered as particularly relevant for such a volume of finite size [4]. Consequently, we seek to identify those statistical characteristics of the ensemble which are important to the material behavior under consideration, and implement microstructure generation algorithms which ensure that generated volume elements reflect those characteristics. The general approach of matching specific statistical microstructure descriptors is well-established in microstructure generation [5] and microstructure reconstruction [6]. For example, for generating fiber-reinforced microstructures, advanced algorithms exist to match the fiber orientation tensors [7,8] and the fiber length distribution of the microstructure [9].

For generating polycrystalline microstructures, a large body of prior work exists. The review article by Bargmann et al. [2] classify polycrystal generators as based on reconstructing experimental data [10], resulting from physics simulations [11], and geometric model approaches. This article focuses on the last type.

The geometry of polycrystalline microstructures is described by an orientation field representing local lattice orientations which are piecewise homogeneous, forming crystallites separated by grain boundaries [2]. The statistical description of a stochastic ensemble of such microstructures involves both the local orientation and its spatial correlations as described by n-point correlation functions [1,12]. From the two-point correlation function of an *individual* microstructure, the microstructure may be reconstructed exactly [13,14], except for some special cases [15]. Given the two-point correlation function of an *ensemble*, the Yeong-Torquato algorithm allows generating finite microstructures with similar statistics [16]. The Yeong-Torquato algorithm is challenging in terms of numerical expense, despite algorithmic improvements in recent years [17]. General microstructure reconstruction approaches like the Yeong-Torquato algorithm encounter the problem that matching the statistics of a stochastic ensemble using a single finite microstructure is not a well-defined problem in general. For example, a single microstructure contains only a finite number of grains, whereas the grain statistics of the ensemble may be continuous functions. Additionally, general approaches using correlation functions do not provide immediate access to some straightforward geometrical properties specific to polycrystals, such as grain size and grain shape. Therefore, specialized polycrystal generation algorithms emerged which describe the morphology in geometric terms, while restricting the orientation statistics to ensure compatibility with an established morphology. We will focus on approaches using one-point statistics, though there are also some which partially incorporate n-point statistics, such as misorientation statistics [18,19].

Prominent methods to describe the microstructure morphology represent crystallites as irregular tiles in spatial tessellations [20] or as particles which are densely packed, followed by a gap-filling process [21]. There is open-source software available to generate microstructures of either type, with Neper [22] implementing tessellations, Kanapy [23] working with dense packings, and Dream.3D [24] implementing both types of methods. Machine-learning methods may also be used for generating polycrystal microstructure generation [25]. All aforementioned methods are capable of reproducing geometrical features such as crystallite shapes and crystallite size distribution, with current research focused on reproducing elongated and irregularly shaped crystallites accurately [26].

The one-point orientation statistics are described by the probability density of individual lattice orientations, which is also known as the Orientation Distribution Function (ODF). In experimental and simulation practice, the ODF is represented by various finite-dimensional approximations. Single-orientation measurement techniques yield experimental data in the form of individual orientations with associated weights [27,28]. The binning method decomposes the orientation space into a finite number of bins [29,30], whose shape and placement may be further optimized [31] based on the underlying texture. The texture component method describes the texture as kernel functions of specified width centered around a finite number of specific points [32,33]. Roe [34] and Bunge [35] introduced the Fourier coefficients of the ODF, also called *texture coefficients*, giving rise to the approach which is used most widely to represent the ODF nowadays.

The Roe and Bunge coefficients are coefficients in the classical sense, i.e., real numbers which depend on a coordinate system convention. A *tensorial* Fourier expansion of the ODF instead yields tensorial texture coefficients, which are coordinate-independent physical quantities [36]. As stated by Guidi et al. [37], the state-variable character of the ODF is properly emphasized using tensorial texture coefficients. The classical texture coefficients are recovered from the tensorial texture coefficients by an appropriate choice of tensorial basis, showing that both approaches are equally expressive [38]. Tensorial texture coefficients play a prominent role in the homogenization theory of linear elasticity [39], i.e., many analytical homogenization schemes allow for an explicit representation in terms of a tensorial texture coefficients up to fourth order [40]. In analytical models of plasticity, higher-order texture are also relevant, e.g., in anisotropic yield functions [41].

The ODF of a tessellation model is given by the discrete lattice orientations, weighted by the crystallite volume fractions. In microstructure generation, the volume fractions are defined by the microstructure morphology parameters, i.e., via a prescribed grain-size distribution. Therefore, when selecting lattice orientations to generate a polycrystal microstructure, the challenge lies in producing a discrete ODF with prescribed weights which yields similar mechanical properties as the prescribed ODF. Random sampling is one such approach, generating discrete ODFs which approximate the prescribed ODF in the infinite-volume limit. With prescribed ODF data from the binning method, the ODF values associated with the bins are interpreted as probability weights, and orientations are sampled as the center points of each bin [30] or as uniformly random orientations within each bin [42,43]. When the ODF is prescribed as a set of texture components, the corresponding kernel functions may be sampled directly [44,45]. As an alternative to random sampling, orientations may be selected in a clever deterministic way [46], which may be combined with a randomization approach [47]. Recently developed orientation selection methods initially generate random samples, then optimize the samples to better correspond to selected statistics of the prescribed ODF. For uniform distributions only, an optimization approach is given by physical analogy to the Thompson problem [48]. Vuppala et al. [49] minimize the L^2-error between a target ODF and

a texture reconstructed from the sampled discrete points, but apply only a single optimization step instead of fully minimizing the error. Liu et al. [50] refine the sampled orientations based on ideal texture components, but the approach is used only for a single ideal component. Finally, Kuhn et al. [51] solve an optimization problem based on matching a finite number of prescribed tensorial texture coefficients.

The problem of finding a discrete set of weighted lattice orientations which approximates another prescribed ODF also arises in microstructure-free crystal plasticity methods [52,53]. In this context, no crystallite weights are prescribed. Consequently, a number of compact ODF representation algorithms emerged which produce sets of orientations with optimally chosen weights [54,55]. Therefore, these methods are not directly applicable to the work at hand, as the volume fractions of the crystallites are pre-specified by sampling from the grain-size distribution of the underlying ensemble. The recent ODF representation algorithm by Marki et al. [56] may be used to generate orientations for preset weights, and is therefore directly applicable to microstructure generation. The strategy consists of solving an optimization problem stated in terms of texture coefficients, like in Kuhn et al. [51]. Marki et al. [56] appear to have discovered the approach independently, leading to slight differences in the strategy: Marki et al. [56] use Bunge coefficients instead of tensorial coefficients, as well as a less powerful optimization algorithm.

As remarked by both Kuhn et al. [51] and Marki et al. [56], the optimization-based approach allows finding small sets of crystallite orientations which can be used to accurately predict the mechanical properties of larger sets of texture data, outperforming methods based on random sampling. How many orientations are required, or indeed, whether an arbitrarily accurate approximation is possible at all, is not known in the general case. For the special case of a uniform ODF, minimal sets of coefficient-matching orientations were found analytically [57]. In general, the number of required orientations increases with the order of considered texture coefficients. Kuhn et al.'s [51] implementation allows prescribing texture coefficients of order up to six, and an extension to higher orders is straightforward in principle. However, due to the large number of algebraic operations involved in dealing with higher-order tensors, the computational effort rises exponentially as the tensor order increases. To accurately simulate material properties which depend on higher-order texture coefficients, more efficient algorithms are required.

1.2. Contributions

We consider the problem of generating representative polycrystal microstructures, with particular emphasis on selecting the lattice orientations of individual grains to match a prescribed texture. We build upon the work by Kuhn et al. [51] and introduce an extension which handles tensorial texture coefficients of arbitrary order in an efficient and accurate way. To validate our results, we apply the novel microstructure generation algorithm to mechanical homogenization of textured polycrystalline materials. More precisely, the following novelties characterize the work at hand:

- Texture coefficient tensors are typically introduced as Fourier coefficients of the ODF [37]. This approach is not general, since the Fourier series associated to some ODFs do not converge. Indeed, the Fourier series converges for an integrable distribution only, ruling out discrete measures, However, when considering a moment-matching problem for the ODF, the texture coefficients emerge naturally. With this shift of perspective, we provide the mathematical foundations for the use of texture tensors in crystallography.
- We introduce the concept of *texture tensors* instead of the commonly used texture coefficients or Guidi et al.'s [37] tensorial texture coefficients. This approach, although evident from a physical point of view, appears to be non-standard. Using texture tensors provides a basis-independent and physically sound measure to quantify texture in polycrystalline materials.
- The original approach by Kuhn et al. [51] is limited to texture tensors of orders four and six. Higher orders come with a computational effort which scales exponentially in the tensor order. We circumvent this problem by working with a harmonic basis [58].
- As an algorithm to solve the texture-coefficient matching problem, we implement the Barzilai–Borwein scheme [59] instead of fixed-step-size gradient descent, further accelerating the procedure compared to the state of the art [51].
- Marki et al. [56] proposed a similar optimization problem to Kuhn et al. [51]. Marki et al. [56] focus on finding discrete sets of orientations with optimized weights, and mention the present case where the weights are given by volume fractions of crystallites in passing. Our investigations focus explicitly on the case where the volume fractions are fixed. Further differences arise in the algorithm used. Whereas Marki et al. [56] use classical texture coefficients and a trust-region solver, we employ an efficient texture tensor implementation and the Barzilai–Borwein method.
- We show that the moment-matching problem for the ODF has a solution. More precisely, for sufficiently large numbers of crystals with sufficiently similar volume fractions, there exists a set of orientations to approximate a prescribed polynomial texture of finite order to arbitrary precision.
- We investigate which texture tensors affect macroscopic mechanical properties using large-scale studies. The effective stiffness of copper shows a slight dependence on sixth-order tensors, despite analytical models taking only tensors up to fourth-order into account [40].
- For the effective yield stress, a dependence up to tenth order emerges, which is the highest order considered. This observation illustrates that higher-order texture terms are relevant for polycrystal microstructure generation algorithms, underlining the relevance of the work at hand.

We describe our algorithm and provide an open-source implementation at https://git.uni-due.de/publicsoftwareingmath/crystallites/ to encourage further study.

1.3. Notation

Throughout the text, we use a symbolic notation for tensor operations. First-order tensors are generally written as bold symbols ($\boldsymbol{v}$), second order as bold capital or Greek symbols ($\boldsymbol{V}$, $\boldsymbol{\sigma}$), and fourth-order tensors as double-struck ($\mathbb{C}$) symbols. For higher and variable-order tensors, the tensor order is indicated explicitly ($\mathbb{V}^n$). The tensor or dyadic product is denoted as $\boldsymbol{A} \otimes \boldsymbol{B}$. We write the single-contraction tensor product between two tensors of second order as $\boldsymbol{AB}$, and between tensors of second and first order as $\boldsymbol{Av}$. A full contraction between two tensors of identical order is written as the dot product $\boldsymbol{A} \cdot \boldsymbol{B}$. Full contractions between a higher and lower-order tensor are written with square brackets $\mathbb{C}[\boldsymbol{\varepsilon}]$. We denote rotations of arbitrary objects by a proper orthogonal rotation tensor $\boldsymbol{R} \in SO(3)$ as $\boldsymbol{R} \star g$, which for tensors resolves to the Rayleigh product, the application of the rotation tensor to every tensorial axis. Also, we use the Kronecker product $\boldsymbol{A} \times \boldsymbol{B}$ and the associated Kronecker power $\boldsymbol{A}^{\times n}$ [60]. Whenever the symbolic notation is not sufficient, we use an index notation with Einstein's summation convention. Tensorial constants used in this work include the second-order identity $(\boldsymbol{I})_{ij} = \delta_{ij}$, the spherical projector $(\mathbb{P}^{\circ})_{ijkl} = \delta_{ij}\delta_{kl}/3$ and the deviatoric projector $(\mathbb{P}')_{ijkl} = \delta_{ik}\delta_{jl}/2 + \delta_{jk}\delta_{il}/2 - \delta_{ij}\delta_{kl}/3$.

2. Random polycrystalline materials, their effective properties and statistical description

2.1. Effective mechanical properties of polycrystals

We consider a stationary and ergodic ensemble of random fields $\mathbb{C} : \mathbb{R}^3 \to C$ of stiffness tensors [61], where C denotes the space of positive definite fourth-order tensors which are both minor- and major-symmetric. For any given stiffness field $\mathbb{C}$, after prescribing the macroscopic strain $\bar{\boldsymbol{\varepsilon}}$, there results a displacement fluctuation field

$$\boldsymbol{u}_{\bar{\varepsilon}} : \mathbb{R}^3 \to \mathbb{R}^3 \tag{2.1}$$

which grows sublinearly and solves the local balance of linear momentum

$$\operatorname{div}\left(\mathbb{C}(\boldsymbol{x})[\bar{\boldsymbol{\varepsilon}} + \nabla^{\mathrm{S}}\boldsymbol{u}_{\bar{\varepsilon}}(\boldsymbol{x})]\right) = \boldsymbol{0}, \quad \boldsymbol{x} \in \mathbb{R}^3. \tag{2.2}$$

Using the effective stress of the ensemble, which is given by the expectation

$$\bar{\boldsymbol{\sigma}} = \langle \mathbb{C}[\bar{\boldsymbol{\varepsilon}} + \nabla^{\mathrm{S}}\boldsymbol{u}_{\bar{\varepsilon}}] \rangle, \tag{2.3}$$

we define the effective stiffness $\bar{\mathbb{C}}$ implicitly using the equation

$$\bar{\mathbb{C}}[\bar{\boldsymbol{\varepsilon}}] = \langle \mathbb{C}[\bar{\boldsymbol{\varepsilon}} + \nabla^{\mathrm{S}}\boldsymbol{u}_{\bar{\varepsilon}}(\boldsymbol{x})] \rangle, \tag{2.4}$$

which holds for any prescribed macroscopic strain $\bar{\boldsymbol{\varepsilon}}$. The effective stiffness $\bar{\mathbb{C}}$ is the quantity of interest in stochastic homogenization [61]. The effective stiffness is computed by defining a basis of strains and computing the effective stress (2.4) for each strain.

One approach to compute effective stresses is computational homogenization, e.g., by using FFT-based methods [62], which generally involve periodized ensembles [63], as the problem (2.2) cannot be solved computationally for an infinite random stiffness field. We consider a stiffness field realization $\mathbb{C}_Y$ on a periodic cubic cell

$$Y = [0, L)^3 \subset \mathbb{R}^3. \tag{2.5}$$

We prescribe the macroscopic strain $\bar{\boldsymbol{\varepsilon}}$ and seek the periodic displacement fluctuation field $\boldsymbol{u}_{Y\bar{\varepsilon}} : Y \to \mathbb{R}^3$ which solves the local balance of linear momentum

$$\operatorname{div}\left(\mathbb{C}_Y(\boldsymbol{x})[\bar{\boldsymbol{\varepsilon}} + \nabla^{\mathrm{S}}\boldsymbol{u}_{Y\bar{\varepsilon}}(\boldsymbol{x})]\right) = \boldsymbol{0}, \quad \boldsymbol{x} \in Y. \tag{2.6}$$

The apparent stress of the microstructure is defined by the volume average

$$\boldsymbol{\sigma}^{\mathrm{app}}_{Y\bar{\varepsilon}} = \frac{1}{L^3}\int_Y \mathbb{C}_Y(\boldsymbol{x})[\bar{\boldsymbol{\varepsilon}} + \nabla^{\mathrm{S}}\boldsymbol{u}_{Y\bar{\varepsilon}}(\boldsymbol{x})]\,\mathrm{d}V(\boldsymbol{x}). \tag{2.7}$$

The apparent stiffness $\mathbb{C}^{\mathrm{app}}_Y$ is implicitly defined by the equation

$$\mathbb{C}^{\mathrm{app}}_Y[\bar{\boldsymbol{\varepsilon}}] = \boldsymbol{\sigma}^{\mathrm{app}}_{Y\bar{\varepsilon}}, \tag{2.8}$$

which holds for all macroscopic strains $\bar{\boldsymbol{\varepsilon}}$. A given periodic cell stiffness field $\mathbb{C}_Y$ is considered *representative* of the ensemble if the apparent stiffness matches the effective stiffness [64]. In practice, we observe random and systematic differences between the apparent and effective stiffness, with both errors depending on the size of the periodic cell Y. Classical results of stochastic homogenization [65] show that under the assumption of ergodicity and stationarity of the ensemble, the apparent stiffness of a sample of limited size L, such as the periodic stiffness field $\mathbb{C}_Y$, converges almost surely towards the effective stiffness as the size L increases [66].

In a single-phase (or uniform) polycrystal, the local stiffness heterogeneity is due to locally differing lattice orientations. In stochastic homogenization of polycrystals, we quantify the local lattice orientation by a random rotation field $\boldsymbol{Q} : \mathbb{R}^3 \to SO(3)$ from a fixed reference lattice orientation r. The local stiffness is then given via a rotation from the stiffness in the reference orientation $\mathbb{C}_{\mathrm{r}}$ as

$$\mathbb{C}(\boldsymbol{x}) = \boldsymbol{Q}(\boldsymbol{x}) \star \mathbb{C}_{\mathrm{r}}, \quad \boldsymbol{x} \in \mathbb{R}^3. \tag{2.9}$$

By Eq. (2.9), the effective stiffness $\bar{\mathbb{C}}$ of the ensemble depends solely on the reference orientation stiffness $\mathbb{C}_{\mathrm{r}}$ and the statistical properties of the random field of orientations $\boldsymbol{Q}$. For the purposes of this work, we focus on the one-point statistics, which take the form of an expected value

$$\langle g \rangle \quad \text{of a continuous function} \quad g : SO(3) \to \mathbb{R}. \tag{2.10}$$

Considering only one-point statistics neglects the influence of spatial correlations of the random orientation field $\boldsymbol{Q}$. In the context of microstructure generation, this restriction decouples the problem of assigning local orientations from the problem of spatially dividing the microstructure into grains [67, section 2.3]. The one-point statistics are fully determined by the orientation distribution function (ODF) $f : SO(3) \to \mathbb{R}$, which is the probability distribution of a given point having the lattice orientation $\boldsymbol{Q}$ [35]. As a probability density, the ODF f is non-negative

$$f(\boldsymbol{Q}) \geq 0, \quad \boldsymbol{Q} \in SO(3), \tag{2.11}$$

and normalized

$$\int_{SO(3)} f(\boldsymbol{Q}) \, \mathrm{d}V(\boldsymbol{Q}) = 1, \tag{2.12}$$

where $\mathrm{d}V$ refers to the Haar measure on the rotation group $SO(3)$, which we assume to be normalized

$$\int_{SO(3)} \mathrm{d}V(\boldsymbol{Q}) = 1. \tag{2.13}$$

The statistics (2.10), which we assume to determine the effective properties of the polycrystal, compute as

$$\langle g \rangle = \int_{SO(3)} g(\boldsymbol{Q}) f(\boldsymbol{Q}) \, \mathrm{d}V(\boldsymbol{Q}). \tag{2.14}$$

As discussed previously, the computational approximation of the effective stiffness (2.4) requires working on cells of finite size (2.5). For such a fixed cell Y, we consider the restricted orientation field $\boldsymbol{Q}_Y : Y \to SO(3)$ and the associated stiffness (2.9)

$$\mathbb{C}_Y(\boldsymbol{x}) = \boldsymbol{Q}_Y(\boldsymbol{x}) \star \mathbb{C}_r. \tag{2.15}$$

Since the cell is finite, only a finite number of grains is contained in such a realization, each grain coming with a homogeneous orientation. For such a discrete set of N orientations $\boldsymbol{Q}_\alpha \in SO(3), \alpha \in \{1, 2, \dots, N\}$, the statistical properties are fully described by the associated volume fractions v_α of the crystallites with orientation $\boldsymbol{Q}_\alpha$, which are positive and normalized

$$v_\alpha > 0, \quad \sum_{\alpha=1}^{N} v_\alpha = 1. \tag{2.16}$$

The discrete statistics induced by functions $g : SO(3) \to \mathbb{R}$ compute as

$$\langle g \rangle_Y = \sum_{\alpha=1}^{N} v_\alpha \, g(\boldsymbol{Q}_\alpha). \tag{2.17}$$

Assuming that the effective properties depend on some statistics $\langle g \rangle$ (2.10), matching the statistics of a periodic microstructure (2.17) to those of a given ensemble (2.14) is a requirement for representativity.

While the above definitions use linear elastic material laws, the same general approach applies to the other constitutive law considered in this work, nonlinear viscoelastoplasticity. Here, the stress field $\boldsymbol{\sigma}$ computes as

$$\boldsymbol{\sigma}(\boldsymbol{x}) = \mathbb{C}(\boldsymbol{x})[\bar{\boldsymbol{\varepsilon}} + \nabla^{\mathrm{S}} \boldsymbol{u}_{\bar{\boldsymbol{\varepsilon}}}(\boldsymbol{x}) - \boldsymbol{\varepsilon}_{\mathrm{p}}(\boldsymbol{x})], \tag{2.18}$$

where the plastic strain field $\boldsymbol{\varepsilon}_{\mathrm{p}}$ depends on the loading history of the material. Assuming that the material initially contains no plastic strains, the heterogeneity of material parameters is again purely due to the local lattice orientation. In both the elastic and elastoviscoplastic case, the microstructure depends on the random orientation field $\boldsymbol{Q}$, and therefore, the statistics $\langle g \rangle$ are of interest.

2.2. Matching the statistics of polycrystals

In the following, we consider the problem of generating a set of orientations matching prescribed statistics $\langle g \rangle_Y$ (2.17). Since we consider a fixed cell, we omit the subscript Y for brevity.

Measure theory provides a formal framework which naturally handles both the continuous ODF (2.12) and the discrete volume fractions (2.16) [58]. To formally describe the one-point orientation probability, we define the probability space $(SO(3), \mathcal{F}, \mu)$, where $\mathcal{F}$ denotes the event space and μ refers to a Borel probability measure which is normalized

$$\int_{SO(3)} \mathrm{d}\mu = 1. \tag{2.19}$$

For example, the Borel measure μ_{iso} – corresponding to a uniform probability distribution – is the normalized Haar measure $\mathrm{d}V(\boldsymbol{Q})$ of $SO(3)$,

$$\int_V \mathrm{d}\mu_{\mathrm{iso}} = \int_V \mathrm{d}V(\boldsymbol{Q}) \quad \text{for all} \quad V \in \mathcal{F}. \tag{2.20}$$

If the probability measure μ is absolutely continuous with respect to μ_{iso}, it corresponds to an ODF via the Radon-Nikodym theorem, i.e., there is an integrable, positive and normalized function f such that the representation

$$\int_V \mathrm{d}\mu(\boldsymbol{Q}) = \int_V f(\boldsymbol{Q}) \, \mathrm{d}\mu_{\mathrm{iso}}(\boldsymbol{Q}) \quad \text{for all} \quad V \in \mathcal{F}. \tag{2.21}$$

is valid.

The probability measure for a discrete set of orientations (2.16) is given by

$$\mu = \sum_{\alpha=1}^{N} v_\alpha \delta_{\boldsymbol{Q}_\alpha}, \tag{2.22}$$

where $\delta_{\boldsymbol{Q}_\alpha}$ denotes the Dirac measure centered at $\boldsymbol{Q}_\alpha$. Such a measure (2.22) is not absolutely continuous, i.e., does not admit an ODF.

Borel measures on a compact topological space are naturally isomorphic with elements of the dual space of the space of continuous functions [68]. As a consequence, two probability measures μ_1 and μ_2 on the compact topological space $SO(3)$ are identical if and only if their integrals

$$\langle \mu_i, g \rangle = \int_{SO(3)} g(\boldsymbol{Q}) \, \mathrm{d}\mu_i(\boldsymbol{Q}) \tag{2.23}$$

against all continuous functions g on the space $SO(3)$ are identical, i.e., the condition

$$\langle \mu_1, g \rangle = \langle \mu_2, g \rangle \tag{2.24}$$

holds for all $g \in C^0(SO(3))$. Generally, a discrete distribution consisting of a finite set of orientations and a continuous distribution cannot be identical, as can be shown by choosing a non-negative function $g \in C^0(SO(3))$ which vanishes in all orientations which are part of the finite set, but is positive on a set of positive measure where the continuous distribution does not vanish. Therefore, a piecewise-constant periodic polycrystal microstructure (2.17) cannot be statistically representative of a general infinite random microstructure (2.10) in the strict sense that all statistics match, i.e., being "structurally entirely typical" as postulated by Hill [69]. However, if the microstructure is only required to be representative with regard to the effective property of interest [64], which depends on some statistics, not all of them, it is sufficient to find discrete distributions which reproduce those statistics exactly.

We discuss this moment-matching problem through the lens of polynomials on $SO(3)$, that is, functions $SO(3) \to \mathbb{R}$ which, after choosing a basis of the vector space of 3×3 matrices $\mathbb{R}^{3\times3} \supset SO(3)$, can be written as multivariate polynomials whose variables are components of the orientation $\boldsymbol{Q}$. Formally, we specify polynomials in a basis-independent manner by choosing an nth order coefficient tensor $\mathbb{A}^n \in (\mathbb{R}^3)^{\otimes n}$ and a basis tensor $\mathbb{B}^n \in (\mathbb{R}^3)^{\otimes n}$ to represent the polynomial

$$p(\boldsymbol{Q}) = \mathbb{A}^n \cdot \boldsymbol{Q} \star \mathbb{B}^n, \tag{2.25}$$

where the Rayleigh product $\boldsymbol{Q} \star \mathbb{B}^n$ denotes the rotation of an nth-order tensor $\mathbb{B}^n$ by the orthogonal tensor $\boldsymbol{Q}$. We will refine the representation (2.25) later, as a given polynomial may be described by *different* tensor pairs $(\mathbb{A}^n, \mathbb{B}^n)$. Furthermore, Eq. (2.25) does not encompass all sums of polynomials. Consequently, we define the set of all polynomials of up to nth order as

$$\mathcal{P}_n = \left\{ p : SO(3) \to \mathbb{R} \mid p(\boldsymbol{Q}) = \sum_{i=1}^{k} \mathbb{A}_i^m \cdot \boldsymbol{Q} \star \mathbb{B}_i^m, \mathbb{A}_i^m \in (\mathbb{R}^3)^{\otimes n}, \mathbb{B}_i^m \in (\mathbb{R}^3)^{\otimes m}, m \le n \right\}, \tag{2.26}$$

i.e., as sums of k polynomials as defined by Eq. (2.25). The set of polynomials of arbitrary order is denoted

$$\mathcal{P}_\infty = \bigcup_{n=0}^{\infty} \mathcal{P}_n. \tag{2.27}$$

The typically considered statistics (2.10) arise as integrals with regard to the ODF-weighted Haar measure μ. Every individual statistics-inducing function g may be approximated to arbitrary precision by polynomials. This fact is well-known. For the convenience of the reader, the arguments are collected in Appendix A. Therefore, it appears natural to investigate polynomial statistics

$$\int_{SO(3)} p_n(\boldsymbol{Q}) \, \mathrm{d}\mu(\boldsymbol{Q}), \tag{2.28}$$

as "universal statistics" – *moments* in the terminology of stochastics. Instead of considering the accuracy of a discretized measure with regard to some unknown micromechanically relevant statistic, we instead evaluate the measure with regard to moments up to a given order. Finding an accurate discretized measure therefore boils down to the following problem:

Moment-matching problem
Given prescribed polynomial statistics up to a degree n (2.28), along with a set of N volume fractions v_α (2.16), find a discrete set of N orientations $\boldsymbol{Q}_\alpha$ to approximate integrals of polynomials up to order n exactly.

This is a classic quadrature problem, except that, usually, when searching for quadrature points $\boldsymbol{Q}_\alpha$, the quadrature weights v_α are not prescribed. In Appendix B, we prove the existence of approximate solutions requiring large numbers of crystallites.

The established technique for the problem of generating discrete orientations is random or pseudo-random sampling [48]. A set of random samples $\{\boldsymbol{Q}_\alpha\}$ of the ODF eventually reproduces all statistics of the ODF, including polynomial statistics of arbitrary degree, as the number of samples tends towards infinity. Using pseudo-random techniques enhances the convergence rate of this process. By contrast, we propose an approach which yields a prescribed number N of quadrature points which are accurate to arbitrary precision in selected polynomial statistics.

2.3. Texture tensors

To compactly describe finite sets of polynomials and their moments, we construct a basis of polynomial functions on $SO(3)$ following the tensorial approach of Guidi et al. [37]. In Eq. (2.26), polynomials are represented by tensor pairs $(\mathbb{A}^n, \mathbb{B}^n)$. Multiple tensor pairs may represent the same polynomial. Indeed, for any index permutation Π, the permuted pair $(\Pi(\mathbb{A}^n), \Pi(\mathbb{B}^n))$ represents the same polynomial as the pair $(\mathbb{A}^n, \mathbb{B}^n)$. Additionally, by multiplying both tensors by the scaled identity tensor $\boldsymbol{I}/\sqrt{3}$, we find

$$\begin{aligned}\left(\mathbb{A}^n \otimes \frac{1}{\sqrt{3}}\boldsymbol{I}\right) \cdot \boldsymbol{Q} \star \left(\mathbb{B}^n \otimes \frac{1}{\sqrt{3}}\boldsymbol{I}\right) &= (\mathbb{A}^n \cdot \boldsymbol{Q} \star (\mathbb{B}^n))\frac{1}{3}(\boldsymbol{I} \cdot \boldsymbol{I}) \\ &= \mathbb{A}^n \cdot \boldsymbol{Q} \star (\mathbb{B}^n) = p(\boldsymbol{Q}),\end{aligned} \tag{2.29}$$

which shows that the pair $(\mathbb{A}^n \otimes \boldsymbol{I}/\sqrt{3}, \mathbb{B}^n \otimes \boldsymbol{I}/\sqrt{3})$ also describes the same polynomial. Guidi et al. [37] avoid this ambiguity by choosing basis tensors which are fully index-symmetric

$$\Pi(\mathbb{B}^n) = \mathbb{B}^n \quad \text{for all index permutations } \Pi, \tag{2.30}$$

and traceless, i.e., vanish upon contraction by the second-order identity tensor $\boldsymbol{I}$

$$\mathbb{B}^n[\boldsymbol{I}] = \mathbb{0}^{n-2}. \tag{2.31}$$

By analogy with the second-order case, we call index-symmetric traceless tensors *deviatoric*. For convenience, we define zeroth- and first-order tensors to be deviatoric tensors as well.

Using methods of group representation theory, it can be shown that the deviatoric tensors of order n comprise a $(2n+1)$-dimensional vector space [70]. If a polynomial representation comprising tensor pairs (2.25) uses deviatoric basis tensors $\mathbb{B}^n$, the corresponding coefficient tensors $\mathbb{A}^n$ can also be assumed to be deviatoric, since the non-deviatoric parts vanish in the dot product.

The question of finding a basis of polynomial functions on the group $SO(3)$ reduces to finding bases for the deviatoric spaces. We construct an orthonormal basis by choosing an arbitrary rotation axis, performing an eigenvector decomposition of the representations of rotations around that axis, and recombining complex-valued eigenvector pairs to obtain a real-valued deviatoric basis [71]. The resulting deviatoric basis tensors are denoted by $\mathbb{D}^n_i, i \in \{1, 2, \dots, 2n+1\}$. Using this basis, a probability measure μ can be quantified using the polynomial moments

$$\mathbb{V}^n_i = \int_{SO(3)} \boldsymbol{Q} \star \mathbb{D}^n_i \, \mathrm{d}\mu(\boldsymbol{Q}), \quad i \in \{1, 2, \dots, 2n+1\}, \tag{2.32}$$

also called tensorial texture coefficients in the literature [37]. For a discrete probability measure μ_d (2.22) with volume fractions v_α and discrete orientations $\boldsymbol{Q}_\alpha$, the moments compute as

$$\mathbb{V}^n_{i,\mathrm{d}} = \sum_{\alpha=1}^{N} v_\alpha \, \boldsymbol{Q}_\alpha \star \mathbb{D}^n_i, \quad i \in \{1, 2, \dots, 2n+1\}. \tag{2.33}$$

The polynomial p^n_i associated with a texture coefficient $\mathbb{V}^n_i$ and a corresponding basis tensor $\mathbb{D}^n_i$ reads

$$p^n_i(\boldsymbol{Q}) = \frac{1}{2n+1}\mathbb{V}^n_i \cdot \left(\boldsymbol{Q} \star \mathbb{D}^n_i\right). \tag{2.34}$$

Using the texture coefficient polynomials as a basis, we may write any mth order polynomial p^m as a sum

$$p^m(\boldsymbol{Q}) = \sum_{n=0}^{m} \frac{1}{2n+1} \sum_{i=1}^{2n+1} \mathbb{V}^n_i \cdot \left(\boldsymbol{Q} \star \mathbb{D}^n_i\right). \tag{2.35}$$

Classically, texture terms of order n are represented using a set of $(2n+1)$ tensorial texture coefficients $\mathbb{V}^n_i$ [37]. However, those tensors depend on the choice of deviatoric basis. This defect is easily repaired by combining all tensorial texture coefficients of order n to define the texture tensor

$$\mathbb{T}^{2n} = \sum_{i=1}^{2n+1} \mathbb{V}^n_i \otimes \mathbb{D}^n_i, \tag{2.36}$$

which permits representing the full polynomial expansion of the ODF in the basis-invariant form

$$p^m(\boldsymbol{Q}) = \sum_{n=0}^{m} \frac{1}{2n+1} \mathbb{T}^{2n} \cdot \boldsymbol{Q}^{\times n}, \tag{2.37}$$

where the Kronecker power $\boldsymbol{Q}^{\times n}$ [60] is used to represent the action of the group $SO(3)$ on nth order tensors

$$\boldsymbol{Q} \star \mathbb{A}^n = \boldsymbol{Q}^{\times n}[\mathbb{A}^n] \quad \text{for all} \quad \mathbb{A}^n \in (\mathbb{R}^3)^{\otimes n}. \tag{2.38}$$

Since the deviatoric tensors $\mathbb{V}^n_i$ and $\mathbb{D}^n_i$ are elements of a $(2n+1)$-dimensional vector space, the texture tensor $\mathbb{T}^{2n}$ can be represented by a $(2n+1) \times (2n+1)$ matrix. If the basis chosen for this representation is the set of basis tensors $\{\mathbb{D}^n_i\}$, the tensorial texture coefficients $\mathbb{V}^n_i$ are recovered as the column vectors of this matrix. The dot product in Eq. (2.37) implies that the Rayleigh action $\boldsymbol{Q}^{\times n}$ may also

be treated as a $(2n+1)\times(2n+1)$ matrix in this context, significantly reducing the number of components compared to a full tensor of order $2n$.

Texture tensors reflect the properties of the ODF (2.12). One direct consequence is that the zeroth-order texture tensor equals unity due to the normalization condition (2.19). Symmetry properties of the ODF apply to the texture tensors as described in Appendix C.

Before moving on to algorithmic details, we provide a short summary. To an arbitrary degree of accuracy, any statistics of the ODF can be represented by a finite set of texture tensors. When generating polycrystal microstructures, matching the texture tensors of the discrete orientations with the ODF leads to microstructures which are statistically representative for polynomial statistics up to a given degree. The discrete orientations are essentially quadrature rules with prescribed weights, which are exact when integrating polynomials up to a specified degree. This ODF-based approach uses only one-point statistics and therefore does not take into account spatial correlations. Compared with random samples of the ODF, orientations which are polynomially exact enhance the statistical representativity of a given microstructure. In computational homogenization, generated microstructures are realizations of a statistical ensemble, which are used to quantify the effective properties. In this context, texture-tensor fitting is a variance reduction approach intended to yield faster convergence of the computed effective properties to the actual effective properties.

3. Generating polycrystalline microstructures

3.1. Problem statement

We consider polycrystal microstructures which consist of crystallites with homogeneous lattice orientations, neglecting defects and presuming infinitely thin crystallite boundaries. The microstructures under consideration are infinitely large and random, forming a statistical ensemble. Computational homogenization, however, requires microstructures of finite volume. Any particular periodic realization contains only a finite number of crystallites instead of the infinite variety of general polycrystalline microstructures. We seek to generate representative finite periodic microstructures corresponding to an ensemble of infinitely large microstructures with known statistical properties.

To represent the microstructure, we use Laguerre tessellations on the cubic domain $Y=[0,L)^3$, which consist of N distinct tiles characterized by seed positions $\boldsymbol{s}_\alpha\in Y$ and weights $w_\alpha\in\mathbb{R}$, where each tile represents a single crystallite. With the periodic distance function

$$d(\boldsymbol{x},\boldsymbol{y})=\min_{\boldsymbol{h}\in\mathbb{Z}^3}\|\boldsymbol{x}-\boldsymbol{y}+Lh_i\boldsymbol{e}_i\|,\quad \boldsymbol{x},\boldsymbol{y}\in Y, \tag{3.1}$$

we define the characteristic function of tile $\alpha\in\{1,2,\dots,N\}$ as

$$I_\alpha(\boldsymbol{x})=\begin{cases}1, & \text{if } d^2(\boldsymbol{x},\boldsymbol{s}_\alpha)-w_\alpha<d^2(\boldsymbol{x},\boldsymbol{s}_\beta)-w_\beta \quad \text{for all} \quad \beta\neq\alpha, \quad \beta\in\{1,2,\dots,N\},\\ 0, & \text{else.}\end{cases} \tag{3.2}$$

Almost every point in Y is associated with one tile via its characteristic function. For points on the boundaries, we choose arbitrary but fixed tiles among those close to the boundary [20]. Each Laguerre tile α has a volume

$$V_\alpha=\int_Y I_\alpha(\boldsymbol{x})\,\mathrm{d}V(\boldsymbol{x}) \tag{3.3}$$

and a volume fraction

$$v_\alpha=\frac{V_\alpha}{L^3}. \tag{3.4}$$

The centroid $\boldsymbol{c}_\alpha$ of a tile α is defined as the point with minimum distance from all points in the tile in an integral sense, i.e., it solves the optimization problem

$$\int_Y d(\boldsymbol{x},\boldsymbol{c}_\alpha)^2 I_\alpha(\boldsymbol{x})\,\mathrm{d}V(\boldsymbol{x})\longrightarrow\min_{\boldsymbol{c}_\alpha\in Y}. \tag{3.5}$$

For tiles which do not intersect the domain boundaries, the tile's centroid is given, as in the non-periodic case, by the center of "mass"

$$\boldsymbol{c}_\alpha=\frac{1}{V_\alpha}\int_Y I_\alpha(\boldsymbol{x})\,\boldsymbol{x}\,\mathrm{d}V(\boldsymbol{x}). \tag{3.6}$$

In Section 2, we discussed the problem of generating discrete orientations which are representative of the ODF. Similarly, we impose conditions on the generated tessellations to reproduce the statistical properties of the ensemble as closely as possible:

- The volume fractions v_α must accurately sample the ensemble's volume fraction distribution $p:[0,1]\to\mathbb{R}$. In terms of the cumulative volume fraction distribution function

$$F:[0,1]\to[0,1]\quad F(v)=\int_0^v p(w)\,\mathrm{d}w, \tag{3.7}$$

this requirement means that

$$\frac{N_{v_\alpha<v}}{N}\to F(v)\quad\text{as}\quad N\to\infty\quad\text{for any}\quad v\in[0,1], \tag{3.8}$$

where $N_{v_\alpha<v}$ denotes the number of samples v_α which are smaller than v.

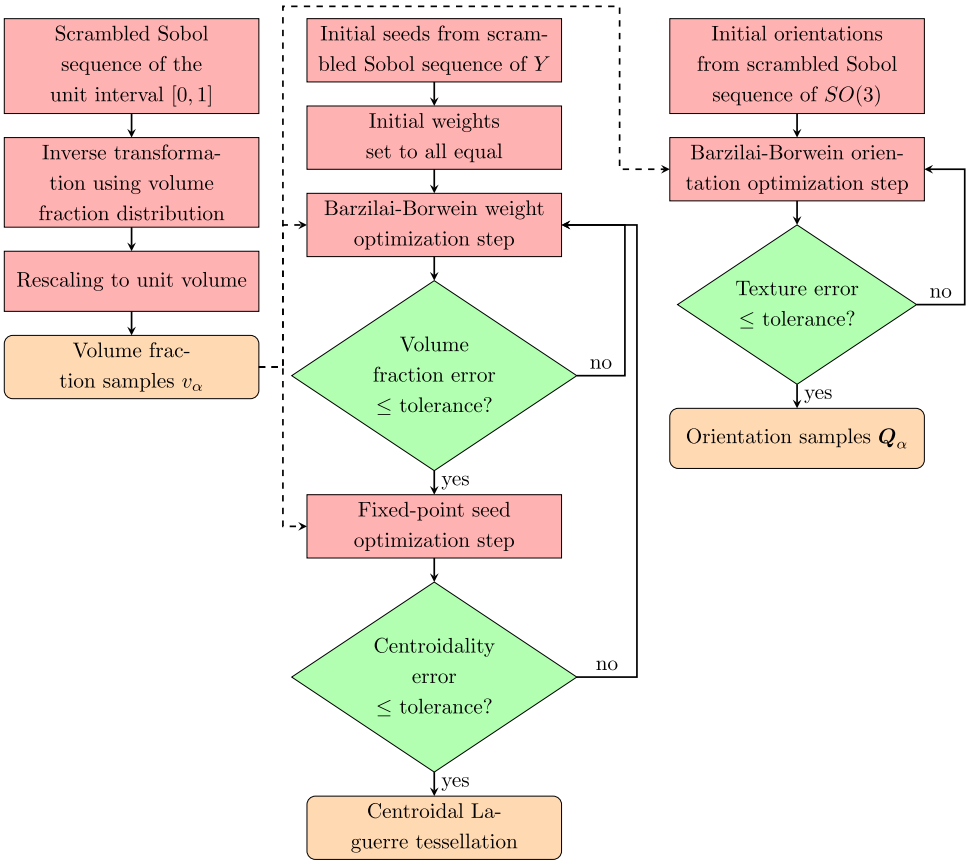

Fig. 1. Overview of the three separate steps involved in the microstructure generation algorithm. From left to right: volume fraction sampling, tessellation sampling, and orientation sampling.

- To enhance shape regularity, we seek centroidal tessellations [72], i.e., tessellations whose centroids equal the seeds

$$\boldsymbol{c}_\alpha = \boldsymbol{s}_\alpha. \tag{3.9}$$

- The tile orientations $\boldsymbol{Q}_\alpha$ must match prescribed texture tensors $\mathbb{V}_i^m$ up to a prescribed order n

$$\sum_{\alpha=1}^{N} \boldsymbol{Q}_\alpha \star \mathbb{D}_i^m = \mathbb{V}_i^m, \quad \text{for all} \quad i \in \{1, 2, \dots, 2m+1\}, \quad m \leq n. \tag{3.10}$$

Our proposed microstructure generation algorithm comprises three steps as illustrated in Fig. 1. Both the tessellation sampling and the orientation sampling depend on prescribed volume fractions, but are independent of each other. More detailed explanations are given in the following.

3.2. Volume fraction sampling

In step 1, we generate samples of the volume fraction distribution. A scrambled Sobol sequence [73] on the interval $[0, 1]$ serves as a set of samples u_α of the uniform probability distribution. We find volume fraction samples using inverse transform sampling

$$v_\alpha^* = F^{-1}(u_\alpha), \tag{3.11}$$

with the cumulative volume fraction distribution F (3.7). Because the generated crystallites need to fill the volume of the periodic cube exactly, we rescale the volume fractions to

$$v_\alpha = \frac{v_\alpha^*}{\sum_{\beta=1}^{N} v_\beta^*}. \tag{3.12}$$

3.3. Tessellation sampling

In step 2, we generate a tessellation that is both centroidal and corresponds to the volume fractions determined in step 1. The centroidality error reads

$$r_c(w_1, \dots, w_N, \boldsymbol{s}_1, \dots, \boldsymbol{s}_N) = \sum_{\alpha=1}^{N} d(\boldsymbol{c}_\alpha, \boldsymbol{s}_\alpha). \tag{3.13}$$

The error in the volume fractions is given by

$$r_v(w_1, \dots, w_N, \boldsymbol{s}_1, \dots, \boldsymbol{s}_N) = \sqrt{\sum_{\alpha=1}^{N} (v_\alpha - v_{\text{target},\alpha})^2}, \tag{3.14}$$

where v_{target} denotes the volume fractions from step 1. Both r_v and r_c depend on the weights and seeds of the Laguerre tessellation, which means that the optimization problems for both errors are coupled. For fixed seeds, finding weights to realize specific volume fractions is a convex optimization problem [20]. For fixed weights, centroidal seeds can be found by Lloyd's fixed-point iteration scheme [72]. We follow Kuhn et al. [74] and combine Lloyd's fixed-point scheme for centroidalization with a Barzilai–Borwein approach to weight optimization in a nested optimization approach. Initially, we assign seeds based on a scrambled Sobol sequence [73] and set all weights to unity. In one outer iteration step, we perform a single step of the fixed-point centroidalizing algorithm, then fit the weights to realize the prescribed volume fractions. We prescribe separate tolerances for volume fractions t_v and centroidality t_c. We terminate the optimization procedure once the condition

$$\max\left(\frac{r_v}{t_v}, \frac{r_c}{t_c}\right) \leq 1 \tag{3.15}$$

is fulfilled. Our algorithm for choosing the tessellation is almost identical to the prior work by Kuhn et al. [74]. The only difference is that we stop the inner weight optimization after only ten steps, regardless of the residual, because exacting precision in weight fitting is unnecessary while the seed position are still imprecise.

3.4. Orientation sampling

In step 3, we generate discrete orientations matching prescribed texture coefficients. For implementation reasons, we use unit quaternions $\boldsymbol{q}$ to represent the orientations. We identify the unit quaternions with unit vectors in $\mathbb{R}^4$, i.e., elements of the three-dimensional unit sphere S^3. We choose basis vectors

$$\boldsymbol{e}_{\text{q}a} \in \mathbb{R}^4, \quad a \in \{1, 2, 3, 4\}, \tag{3.16}$$

such that $\boldsymbol{e}_{\text{q}1}$ represents a purely real quaternion. The projection from the quaternion unit vector onto the vector of non-real components reads as a mixed tensor

$$\boldsymbol{P} \in \mathbb{R}^3 \otimes \mathbb{R}^4, \quad \boldsymbol{P} \hat{=} \begin{pmatrix} 0 & 1 & 0 & 0 \\ 0 & 0 & 1 & 0 \\ 0 & 0 & 0 & 1 \end{pmatrix}_{(\boldsymbol{e}_i, \boldsymbol{e}_{\text{q}j})}. \tag{3.17}$$

The relationship between orientation tensors and quaternions is given by the formula

$$\boldsymbol{Q} = \mathbb{P}_{\text{Q}}[\boldsymbol{q} \otimes \boldsymbol{q}] \tag{3.18}$$

with the constant (3,3,4,4)-dimensional tensor $\mathbb{P}_{\text{Q}}$ given by

$$\mathbb{P}_{\text{Q}} = \boldsymbol{I} \otimes \boldsymbol{e}_{\text{q}1} \otimes \boldsymbol{e}_{\text{q}1} - 2\epsilon \boldsymbol{P} \otimes \boldsymbol{e}_{\text{q}1} + \left(\mathbb{P}' - \mathbb{P}^\circ\right)(\boldsymbol{P} \times \boldsymbol{P}), \tag{3.19}$$

or in index notation,

$$P^{\text{Q}}_{ijab} = \delta_{ij}\delta_{1a}\delta_{1b} - 2\epsilon_{ijk}P_{ka}\delta_{1b} + \left(P'_{ijkl} - P^\circ_{ijkl}\right)P_{ka}P_{lb}, \tag{3.20}$$

where indices starting from i take values from one to three, and indices a, b take values from one to four. This is a tensorial form of the well-known relationship between quaternions and rotation matrices, which is usually stated in component form Shepperd [75].

To generate an initial set of orientations, we sample the uniform distribution. For a start, we generate pseudo-random samples of the uniform distribution on the hypercube $[0, 1]^4$ using a scrambled Sobol sequence. Each component of that four-dimensional uniform distribution is transformed using the inverse cumulative distribution function of the standard normal distribution. The uncorrelated four-dimensional multivariate normal distribution has isotropic statistics. Therefore, if we project the multivariate normal samples onto the four-dimensional embedding of the unit sphere $S^3 \in \mathbb{R}^4$, we obtain a uniform sampling of the unit sphere S^3 [76]. By the relationship between orientation tensors and quaternions (3.18), we obtain samples of the uniform distribution on $SO(3)$.

We define the square texture coefficient error [51] up to order $n_{\max}$

$$r : SO(3)^N \to \mathbb{R}, \quad r(\boldsymbol{Q}_1, \boldsymbol{Q}_2, \dots, \boldsymbol{Q}_N) = \sum_{n=0}^{n_{\max}} \sum_{j=1}^{2j+1} \left\| \mathbb{V}_j^n - \sum_{\alpha=1}^{N} v_\alpha \boldsymbol{Q}_\alpha \star \mathbb{D}_j^n \right\|^2. \tag{3.21}$$

To match the orientation samples $\boldsymbol{Q}_\alpha$ to the prescribed texture coefficients $\mathbb{V}_j^n$, we minimize

$$r(\boldsymbol{Q}_1, \boldsymbol{Q}_2, \dots, \boldsymbol{Q}_N) \to \min_{\boldsymbol{Q}_\alpha \in SO(3)}. \tag{3.22}$$

The objective function (3.21) is a polynomial on the N-fold product space $SO(3)^N$. Due to the index symmetry of the deviatoric basis tensors $\mathbb{D}_j^n$, its derivative simplifies to

$$\frac{\partial r(\boldsymbol{Q}_1, \boldsymbol{Q}_2, \dots, \boldsymbol{Q}_N)}{\partial \boldsymbol{Q}_\alpha} = \sum_{n=0}^{n_{\max}} \sum_{j=1}^{2j+1} \left(\mathbb{V}_j^n - \sum_{\beta=1}^{N} v_\beta \boldsymbol{Q}_\beta \star \mathbb{D}_j^n \right) \overset{(n-1)}{\cdot} \left(v_\alpha n (\boldsymbol{Q}_\alpha^{\times(n-1)} \times \boldsymbol{I})[\mathbb{D}_j^n] \right), \tag{3.23}$$

where the operation $\overset{(n-1)}{\cdot}$ denotes an $(n-1)$-fold tensor contraction.

Computing the objective function and its gradient becomes increasingly numerically expensive for a high tensor order n. A direct calculation of the term $\boldsymbol{Q} \star \mathbb{D}_j^n$, implemented via successive matrix multiplications of the orientation matrix Q_{ij} and the component array $D^n_{ijkl\dots}$ requires one matrix multiplication for each tensor axis, which in total necessitate $3^{n+1}n$ floating-point operations [71]. Instead, we may as in Eq. (2.38) compute rotations using the Kronecker power $\boldsymbol{Q}^{\times n}$ and exploit its sparsity. The tensor $\mathbb{D}_j^n$ is an element of the nth order deviatoric tensor space, which is an eigenspace of $\boldsymbol{Q}^{\times n}$. It is therefore sufficient to represent the tensor $\boldsymbol{Q}^{\times n}$ by its deviatoric components

$$\left(\boldsymbol{Q}^{\times n}\right)_{jk} = \boldsymbol{Q}^{\times n} \cdot (\mathbb{D}_j^n \times \mathbb{D}_k^n), \tag{3.24}$$

which form a $(2n+1) \times (2n+1)$-dimensional matrix. The numerical effort of this matrix-vector multiplication is quadratic in the order n, and the asymptotic efficiency bottleneck is caused by the calculation of the deviatoric rotation matrix. To compute the matrix $\left(\boldsymbol{Q}^{\times n}\right)_{jk}$, we use a basis transformation from Wigner-d-symbols [71]. The computation of Wigner-d symbols is possible with an asymptotic complexity of $\mathcal{O}(n^3)$ using the algorithm by Dachsel [77]. By exploiting the sparsity of the rotation matrix $\left(\boldsymbol{Q}^{\times n}\right)_{jk}$, we therefore reduce the asymptotic complexity of evaluating the objective function from $\mathcal{O}(3^n)$ to $\mathcal{O}(n^3)$. Effectively, the sparse matrix representation of the rotation matrix allows us to overcome the computational inefficiency of using full tensorial texture coefficients, in the process recovering the computational efficiency of classical texture coefficients [34,35] in the tensorial setting.

In the expression for the gradient (3.23), a similar multiplication by the $\boldsymbol{Q}^{\times n-1}$-tensor appears. We efficiently implement this operation by first transforming the tensor $\mathbb{D}_j^n$ into the mixed $\mathbb{D}_j^{n-1} \otimes \boldsymbol{D}_k^1$ basis, which reads

$$(\mathbb{D}_j^n)_{kl} = \mathbb{D}_j^n \cdot (\mathbb{D}_k^{n-1} \otimes \boldsymbol{D}_l^1). \tag{3.25}$$

Using the Clebsch-Gordan decomposition, the right-hand side of Eq. (3.25) arises as the jkl-component of the Clebsch-Gordan tensor $\mathbb{C}^{n,n-1,1}$ [71]. On the matrix of Clebsch-Gordan components, the gradient rotation tensor acts via the matrix-matrix product

$$\left((\boldsymbol{Q}_\alpha^{\times(n-1)} \times \boldsymbol{I})[\mathbb{D}_j^n] \right)_{km} = (\boldsymbol{Q}_\alpha^{\times(n-1)})_{kl} \left(\mathbb{D}_j^n \right)_{lm}. \tag{3.26}$$

The objective function from Eq. (3.21) is expressed in terms of quaternions as

$$r_{\mathrm{q}}(\boldsymbol{q}_1, \boldsymbol{q}_2, \dots, \boldsymbol{q}_N) = r(\mathbb{P}_{\mathrm{Q}}[\boldsymbol{q}_1 \times \boldsymbol{q}_1], \dots, \mathbb{P}_{\mathrm{Q}}[\boldsymbol{q}_N \times \boldsymbol{q}_N]), \tag{3.27}$$

and the gradient $\boldsymbol{g}$ of r_{q} follows via the chain rule

$$\boldsymbol{g}_\alpha = \frac{\partial r_{\mathrm{q}}(\boldsymbol{q}_1, \dots, \boldsymbol{q}_N)}{\partial \boldsymbol{q}_\alpha} = \mathbb{P}_{\mathrm{Q}}^{\mathsf{T}} \left[\boldsymbol{q} \otimes \frac{\partial r(\boldsymbol{Q}_1, \dots, \boldsymbol{Q}_N)}{\partial \boldsymbol{Q}_\alpha} \right]. \tag{3.28}$$

To minimize the objective function, we use the Barzilai–Borwein method [59]. For step k, the linear increment of the quaternion $\boldsymbol{q}_\alpha$ is computed from the quaternion gradient $\boldsymbol{g}_\alpha$ (3.28) via

$$\Delta \boldsymbol{q}_\alpha^{k+1} = s^k \, \boldsymbol{g}_\alpha^k, \tag{3.29}$$

where the step size s^k is given by

$$s^k = -\frac{\sum_{\alpha=1}^{N} \Delta \boldsymbol{q}_\alpha^k \cdot \Delta \boldsymbol{q}_\alpha^k}{\sum_{\alpha=1}^{N} \Delta \boldsymbol{g}_\alpha^k \cdot \Delta \boldsymbol{q}_\alpha^k} \tag{3.30}$$

with

$$\Delta \boldsymbol{g}_\alpha^k = \boldsymbol{g}_\alpha^k - \boldsymbol{g}_\alpha^{k-1}, \tag{3.31}$$

$$\Delta \boldsymbol{q}_\alpha^k = \boldsymbol{q}_\alpha^k - \boldsymbol{q}_\alpha^{k-1}. \tag{3.32}$$

Because the optimization takes place on the unit sphere S^3, not the ambient vector space $\mathbb{R}^4$, the updated value $\boldsymbol{q}_\alpha^{k+1}$ of the quaternion is not computed via straightforward addition, but requires taking the geometry of the Riemannian manifold S^3 into account [78]. We project the quaternion increment (3.29) to the tangent space at $\boldsymbol{q}_\alpha$ using the formula

$$\Delta \tilde{\boldsymbol{q}}_\alpha^{k+1} = \Delta \boldsymbol{q}_\alpha^{k+1} - \left(\Delta \boldsymbol{q}_\alpha^{k+1} \cdot \boldsymbol{q}_\alpha^k \right) \boldsymbol{q}_\alpha^k. \tag{3.33}$$

The additive tangent space increment is mapped to a multiplicative manifold increment using the exponential map relating the tangent space with the manifold S^3 [79]. The updated value of the quaternion $\boldsymbol{q}_\alpha$ computes as

$$\boldsymbol{q}_\alpha^{k+1} = \cos(\|\Delta \tilde{\boldsymbol{q}}_\alpha^{k+1}\|) \, \boldsymbol{q}_\alpha^k + \frac{\sin(\|\Delta \tilde{\boldsymbol{q}}_\alpha^{k+1}\|)}{\|\Delta \tilde{\boldsymbol{q}}_\alpha^{k+1}\|} \Delta \tilde{\boldsymbol{q}}_\alpha^{k+1}. \tag{3.34}$$

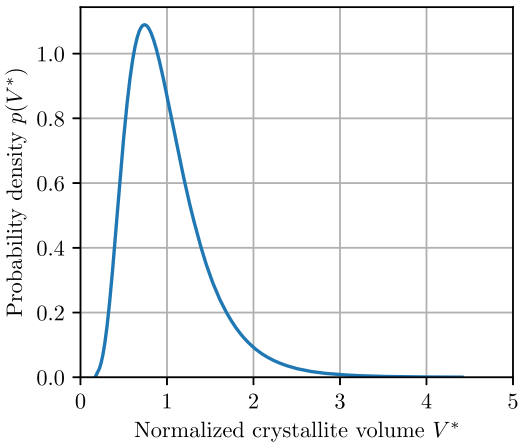

Fig. 2. Normalized crystallite volume distribution used for the example material.

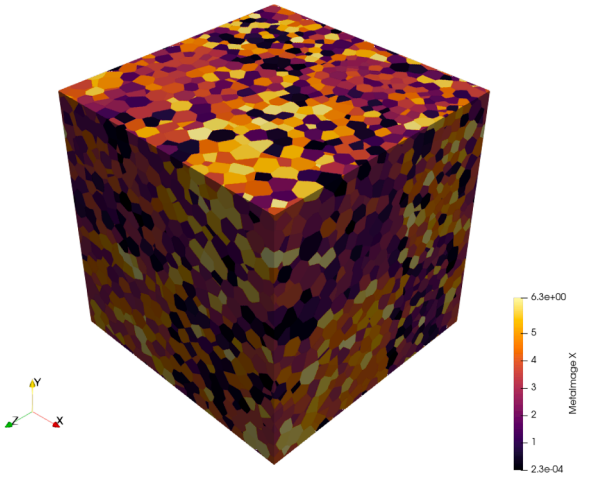

Fig. 3. Realization of the example material with 8192 crystallites resolved using 512^3 voxels. Colors show the first Euler angle.

Table 1
Material parameters for viscoplastic simulations of copper.

Cubic stiffness	C_{1111} 170.2 GPa	C_{1122} 114.9 GPa	C_{1212} 61.0 GPa	
Flow rule	$\dot{\gamma}_0$ 0.001 s^{-1}	τ_F 12 MPa	τ_D 4 MPa	m 20

4. Computational investigations

4.1. Example microstructure

We investigate microstructure generation for polycrystalline copper. For the probability distribution of crystallite equivalent diameters, we assume a log-normal distribution, as typically observed in experimental results [80]. Following Kuhn et al. [51], we set the mean of the log-normal distribution to unity and assume a standard deviation of

$$\sqrt{\langle D^2\rangle - \langle D\rangle^2} = 0.15. \tag{4.1}$$

The crystallite volume V is related to the equivalent diameter D by the relation

$$V = \frac{\pi}{6} D^3. \tag{4.2}$$

The logarithm of a log-normally distributed value is normally distributed with mean μ and standard deviation σ. The corresponding parameters of the volume distribution read

$$\mu_V = \log\left(\frac{\pi}{6}\right) + 3\mu_D, \tag{4.3}$$

$$\sigma_V = 3\sigma_D. \tag{4.4}$$

The mean and standard deviation of a log-normally distributed value compute as

$$\langle V\rangle = \mu_V + \frac{\sigma_V^2}{2}, \tag{4.5}$$

$$\sqrt{\langle V^2\rangle - \langle V\rangle^2} = \sqrt{\left(\exp\left(\sigma_V^2\right) - 1\right)\exp\left(2\mu + \sigma^2\right)}. \tag{4.6}$$

We re-normalize the volume distribution to a mean of 1, leading to a standard deviation of roughly

$$\sqrt{\langle (V^*)^2\rangle - \langle V^*\rangle^2} = 0.15. \tag{4.7}$$

This distribution is illustrated in Fig. 2.

We consider copper with a rolling texture as obtained after cold-rolling to a thickness reduction of 28 %. The texture data was obtained in a previous work [81], using a Taylor–Lin [82,83] texture simulation, i.e., by prescribing a homogeneous deformation process to initially randomly oriented crystallites. The material model used is slip-based crystal plasticity with the slip systems

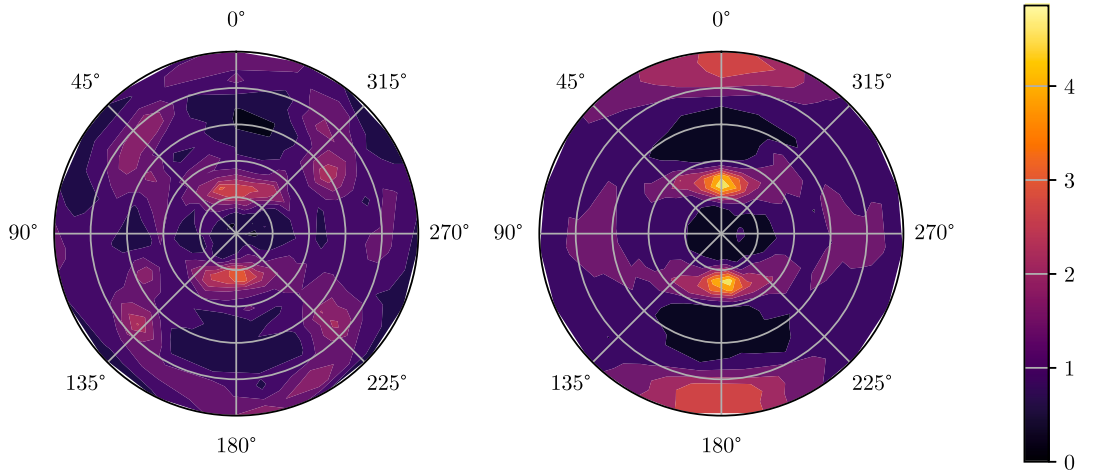

Fig. 4. Copper rolling texture pole figures based on samples interpolated with a Mises–Fischer Kernel and a half-width of 5°.

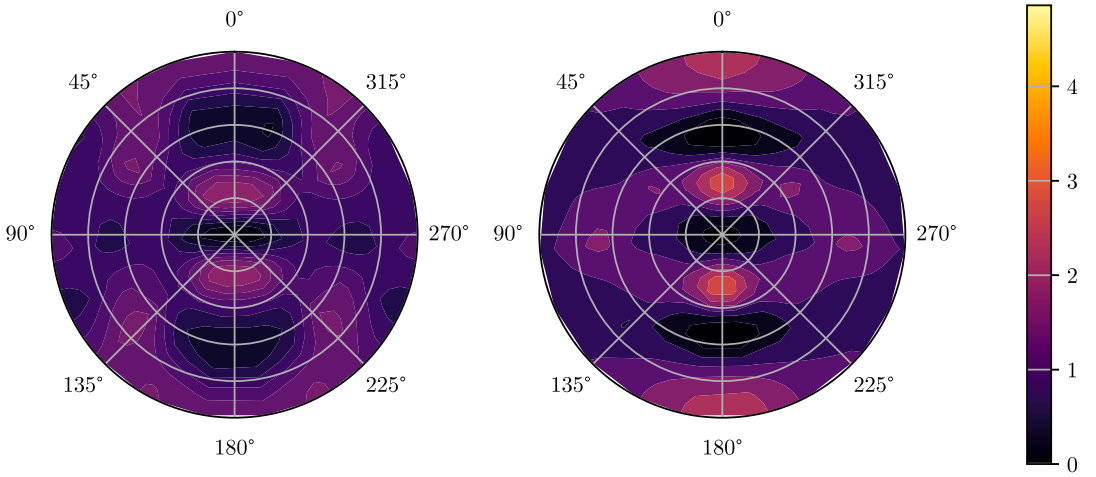

Fig. 5. Pole figures reconstructed using texture coefficients of order up to 10.

{111}⟨110⟩, as is typical for an FCC lattice. The slip rate $\dot{\gamma}_\alpha$ in system α is modeled using a Chaboche model [84],

$$\dot{\gamma}_\alpha = \dot{\gamma}_0 \operatorname{sgn}(\tau_\alpha) \left\langle \frac{|\tau_\alpha| - \tau_\mathrm{F}}{\tau_\mathrm{D}} \right\rangle^m . \tag{4.8}$$

Material parameters for the Chaboche slip rate and the elastic stiffness with respect to the single crystal lattice vectors are given in Table 1. For the viscoplastic large-deformation simulation, hardening is neglected. For more details on the Taylor–Lin texture simulation, we refer to the more detailed explanation in the work [81].

The texture simulations result in 11 000 discrete orientations representing the rolled copper texture. To obtain a continuous ODF for visualization purposes, we interpolate the discrete measure (2.22) with a Mises–Fisher kernel

$$f_\alpha(\boldsymbol{Q}) = \frac{\exp\left(\kappa \boldsymbol{Q}_\alpha \cdot \boldsymbol{Q}\right)}{\int_{SO(3)} \exp\left(\kappa \boldsymbol{Q}_\alpha \cdot \boldsymbol{Q}\right) \mathrm{d}\mu_\mathrm{iso}}, \quad \kappa = \frac{\log(2)}{1 - \cos(w)}, \tag{4.9}$$

with a half-width $w = 5°$. We visualize the interpolated texture by computing (1,0,0) and (1,1,1) pole figures, which are stereographic projections of the ODF values associated with the (1,0,0) and (1,1,1) lattice vectors, respectively [85]. The resulting figures are shown in Fig. 4, with the rolling direction at 0°. Note that the pole figures exhibit the typical texture expected of pure copper [86].

Table 2
Computational effort of generating the baseline microstructure.

Sampled property	Volume fractions	Orientation	Tessellation
Total time	0.001 s	25.4 s	82.8 s
Optimization steps	–	37	26 (outer) and 251 (inner)

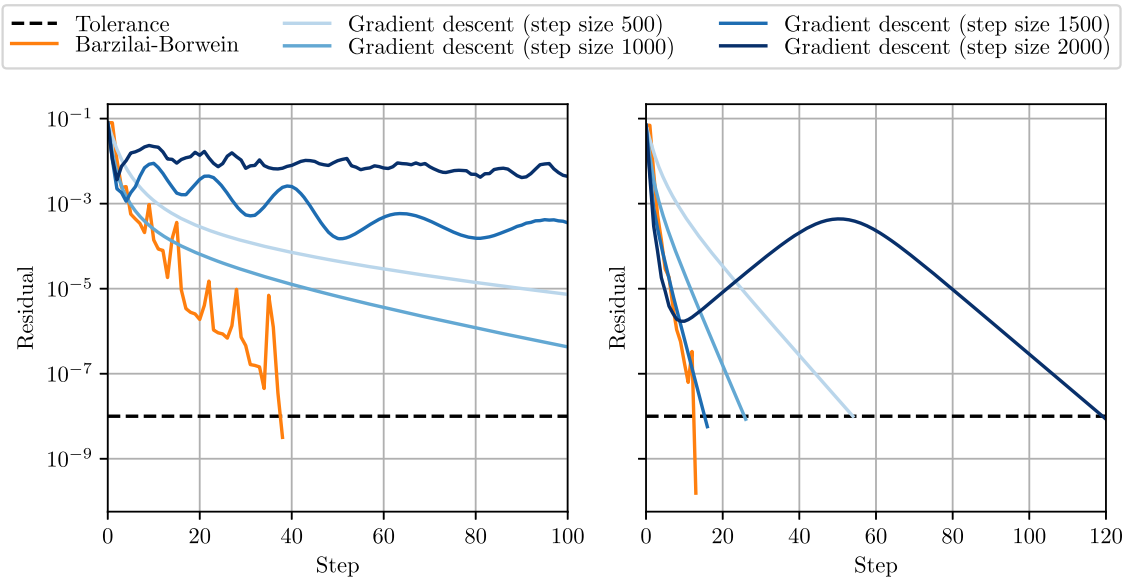

Fig. 6. Convergence behavior of texture coefficient error minimization for the Barzilai–Borwein method compared to a gradient descent algorithm with a step size of 500, 1000, 1500 or 2000. On the left, convergence is shown for the baseline microstructure parameters, while on the right, only texture coefficients up to sixth order are prescribed.

As discussed in Section 2, this texture can be approximately quantified as a finite set of texture tensors. We use cubic deviatoric basis tensors up to tenth order as listed in Appendix D, and compute texture coefficients directly from the samples using Eq. (2.33). For visualization purposes, we use the polynomials (2.37) to reconstruct approximate pole figures as shown in Fig. 5. Note that in this visualization, we assume all texture coefficients of higher order are zero, which is not the case for the real samples or the microstructures which will be generated in the following. Nonetheless, the visualization is sufficient to observe that the set of cubic polynomials up to order ten seems to approximate the pole figures of the interpolated texture well enough to reproduce salient features.

4.2. Performance of the microstructure generation algorithm

We investigate the performance of the microstructure generation algorithm in terms of total time and steps taken. All time measurements were recorded on a laptop computer with an Intel i7 CPU and 64 GB RAM. As the code is not parallelized, only one core is used.

We begin by evaluating the microstructure generator for the copper material discussed in the previous section. We generate a 8192-crystallite-microstructure with a normalized volume standard deviation of 0.47 and prescribed texture coefficients up to order ten, as illustrated in Fig. 3. The tolerance of the texture coefficient error is set to 10^{-8}, for the weight error to 10^{-5}, and for the centroidality error to 10^{-4}. The computational effort to achieve these tolerances is summarized in Table 2. The volume fraction sampling, involving no optimization, takes negligible time. Both orientation and tessellation sampling require double-digit seconds. As the tessellation optimization procedure we use was investigated in detail by Kuhn et al. [74], we focus on the impact of various optimization parameters on the orientation sampling.

For orientation sampling, we compare the Barzilai–Borwein optimization algorithm with the gradient descent algorithm. For the gradient descent algorithm, we choose four different step size values, 500, 1000, 1500 and 2000. As illustrated in Fig. 6, the convergence speed of the gradient descent algorithm increases with the step size, until a critical value is reached, for which convergence is no longer monotonic. For prescribed texture coefficients up to tenth order, a step size of 1500 exceeds that critical value, while for texture coefficients up to sixth order, it is the quickest choice among those investigated. We conclude that the choice of step size is critical and depends in a complex manner on the problem parameters. The Barzilai–Borwein method avoids the problem of choosing a fixed step size. As can be seen particularly for the baseline microstructure, there does not necessarily exists an optimal fixed step size,

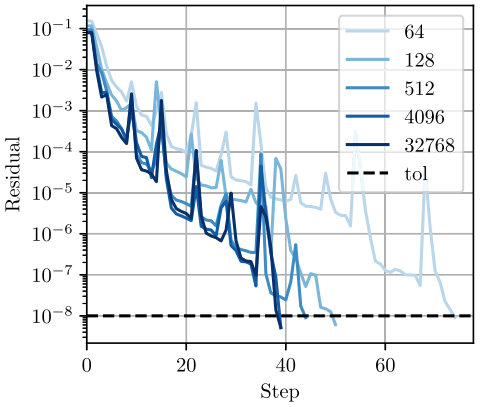

Fig. 7. Convergence behavior of the orientation sampling procedure for the example material with different numbers of crystallites.

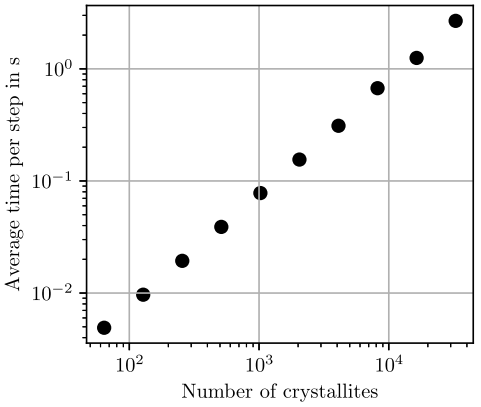

Fig. 8. Computation time per orientation optimization step depending on the number of crystallites.

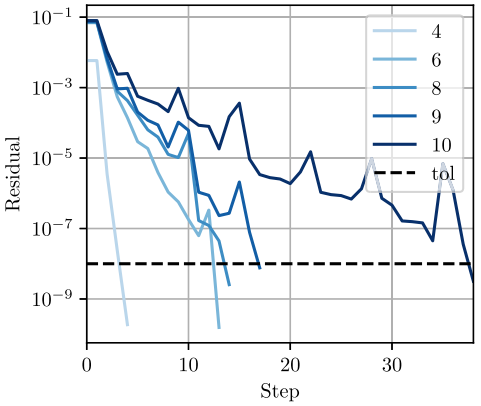

Fig. 9. Convergence behavior of the orientation sampling procedure for different prescribed texture orders.

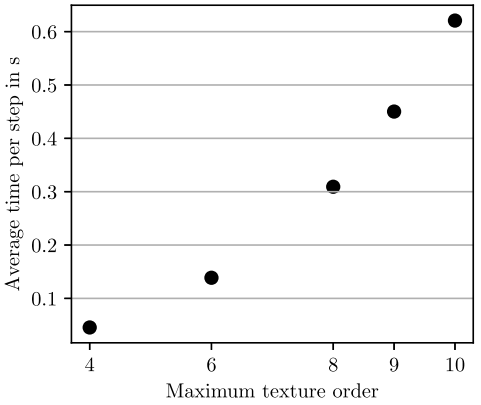

Fig. 10. Computation time per orientation optimization step depending on the prescribed texture order.

such that the adaptable step size of the Barzilai–Borwein method is a major advantage. In all considered cases, the Barzilai–Borwein method leads to convergence in the fewest steps.

In Fig. 7, the convergence behavior of the orientation optimization problem is shown for different numbers of crystallites. The microstructure with the lowest amount of crystallites, 64, takes 74 steps to convergence, as the few crystallites present are heavily constrained by the prescribed texture coefficients up to order ten. With increasing numbers of crystallites, convergence becomes easier to achieve. Above roughly 500 crystallites, no further significant reduction in steps taken is observed. As shown in Fig. 8, the time required for each optimization step increases linearly in the number of crystallites.

Next, we consider the influence of the prescribed texture coefficients. As discussed in Section 3.4, the algebraic operations involved in both the residual and the gradient calculations are asymptotically cubic in the tensor order. This cubic relationship holds for the finite tensor orders under consideration as well, as shown in Fig. 10. The texture order also influences the convergence behavior, as shown in Fig. 9. Prescribing additional texture tensors excludes previously viable solutions. As the set of solutions shrinks, more steps are required to reach convergence.

In addition to texture order, the convergence behavior is influenced by texture strength. We decrease the sharpness of the texture by scaling each texture coefficient by the factor $\theta \in [0, 1]$. In terms of the probability measure μ, this is equivalent to a convex combination of the existing measure with the isotropic measure, weighted as

$$\mu(\theta) = \theta \mu_{\text{copper}} + (1 - \theta)\mu_{\text{iso}}. \tag{4.10}$$

In Fig. 11, the number of required steps to convergence is shown to decrease with a decreasing texture anisotropy factor θ.

Finally, we discuss the influence of grain size variance. For the tessellation sampling procedure, increasing the grain size variance has a large effect on the number of optimization steps [74]. For the baseline microstructure example with a normalized volume standard deviation of 0.47, we observe that a total of 251 inner optimization steps are required. If the standard deviation vanishes,

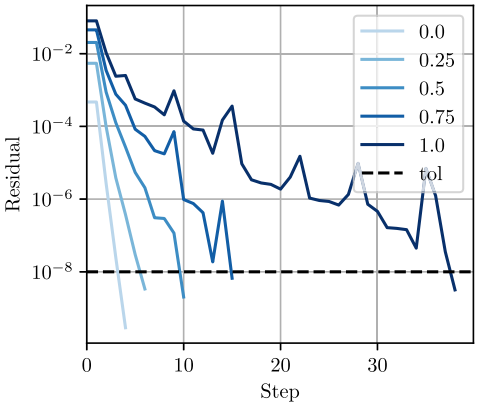

Fig. 11. Convergence behavior of the orientation sampling procedure given different texture strengths θ (4.10).

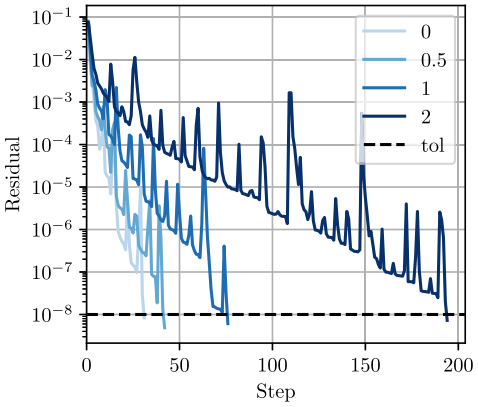

Fig. 12. Orientation optimization convergence for different normalized grain volume standard deviations (4.7).

yielding an equal-sized grain distribution, only 6 outer steps and 17 inner steps are necessary to reach the same centroidality and weight tolerances. However, the number of orientation optimization steps remains roughly the same, decreasing from 37 to 30. In Fig. 12, the optimization convergence is shown for the baseline microstructure parameters and three different standard deviations. We note that convergence is reached even for a normalized volume standard deviation of 2, for which the randomly generated volume fraction samples span eight orders of magnitude.

4.3. Elastic homogenization

We investigate the influence of texture coefficients on the effective stiffness of a linear elastic polycrystal. Since the convergence rate of the orientation sampling procedure appears to depend heavily on the number of prescribed texture coefficients, we seek to find out whether some higher-order texture coefficients can be neglected when generating microstructures for linear elastic homogenization. As an example material, we use copper with the stiffness given in Table 1. The microstructures under consideration are centroidal Laguerre tessellations generated using the algorithm described in Section 3. Each microstructure is converted to a voxel representation by evaluating the characteristic function (3.2) on an equally-spaced grid.

We compute the apparent stiffness (2.8) of the generated microstructures using an in-house numerical homogenization code based on the fast-Fourier-transform (FFT) method. The local stress and strain fields are discretized using the staggered grid discretization [87]. To solve the discretized system, we use the conjugate gradient method [88]. For each microstructure, we perform six simulations with applied strains that are pairwise orthogonal to each other, then reconstruct the effective stiffness from the computed effective stresses.

Before investigating the influence of texture coefficients, we perform a resolution study using microstructures with prescribed vanishing texture coefficients up to order ten. As no non-vanishing texture coefficients are prescribed, in the infinite-volume limit, the microstructures reach an isotropic orientation probability measure μ_{iso}, which we take as the ground truth of this resolution study. For symmetry reasons, the ground truth effective stiffness is isotropic. Because the compressive behavior of a cubic single crystal is independent of its orientation, the effective compression modulus is directly available from the local stiffness properties as

$$\bar{K} = \frac{1}{3}\left(C_{1111} + 2C_{1122}\right). \tag{4.11}$$

The effective shear modulus of the ground truth ensemble is not known, which is why we approximate it as the apparent shear modulus of a microstructure consisting of 16 384 crystallites discretized using 1024 voxels each, for a total resolution of 256^3 voxels. We compute this effective shear modulus by projecting the stiffness via

$$\bar{G} = \frac{1}{10}\bar{\mathbb{C}} \cdot \mathbb{P}'. \tag{4.12}$$

We define the relative stiffness error of a computationally homogenized apparent stiffness $\bar{\mathbb{C}}_{\text{app}}$ as

$$e = \frac{\|\bar{\mathbb{C}}_{\text{app}} - \bar{\mathbb{C}}\|}{\|\bar{\mathbb{C}}_{\text{app}}\|}. \tag{4.13}$$

The apparent stiffness naturally splits into an isotropic projection and an anisotropic part,

$$\mathbb{C}_{\text{app,iso}} = 3\bar{K}\mathbb{P}^{\circ} + \frac{\bar{\mathbb{C}}_{\text{app}} \cdot \mathbb{P}'}{5}\mathbb{P}', \tag{4.14}$$

$$\mathbb{C}_{\text{app,aniso}} = \mathbb{C}_{\text{app}} - \mathbb{C}_{\text{app,iso}}. \tag{4.15}$$

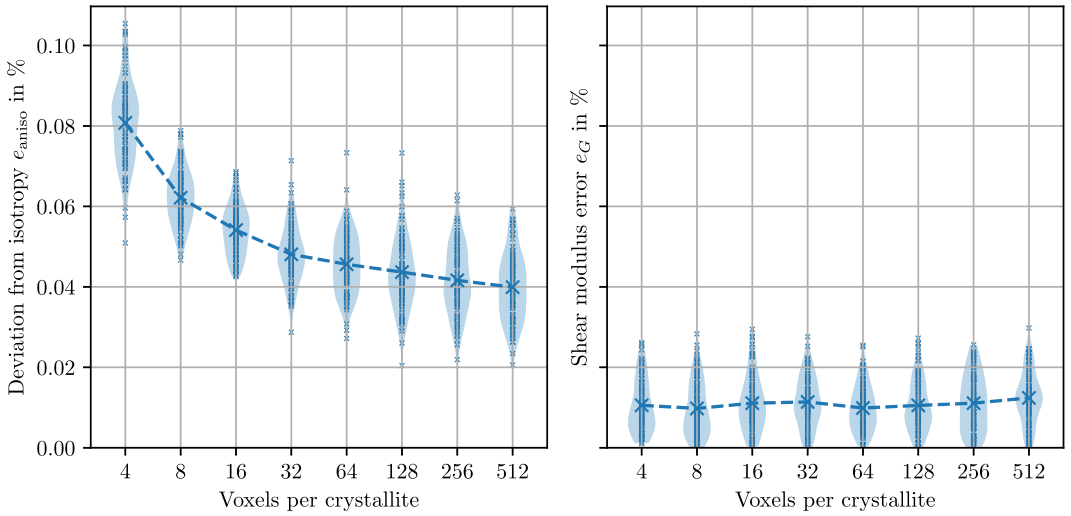

Fig. 13. Deviation from isotropy (left) and shear modulus error (right) for microstructures with 8192 crystallites and varying numbers of voxels per crystallite, with 100 realizations each. The reference shear modulus for the shear modulus error is obtained from one simulation with 16,384 crystallites using a resolution of 1024 voxels per crystallite.

In our simulations, we find that the apparent compression modulus $\bar{K}$ is identical for all simulations to within the tolerance of the solver, as expected in light of Eq. (4.11). Based on the stiffness decomposition, we define the shear modulus error and the deviation from isotropy,

$$e_G = \frac{\|\mathbb{C}_{\text{app,iso}} - \bar{\mathbb{C}}\|}{\|\mathbb{C}_{\text{app}}\|} = \frac{2\sqrt{5}|\bar{G}_{\text{app}} - \bar{G}|}{\|\mathbb{C}_{\text{app}}\|}, \tag{4.16}$$

$$e_{\text{aniso}} = \frac{\|\mathbb{C}_{\text{app,aniso}}\|}{\|\mathbb{C}_{\text{app}}\|}. \tag{4.17}$$

We note that the deviation from isotropy does not depend on the reference stiffness.

We begin with a resolution study. As shown in Fig. 13, the mean deviation from isotropy is roughly 0.08 % for microstructures with as few as four voxels per crystallite. With increasing resolution, the deviation from isotropy decreases further to around 0.04 %. The mean shear modulus error is significantly lower at roughly 0.01 %, and does not decrease significantly with increasing resolution. Presumably, a higher number of crystallites, e.g., a larger cell size, would be required to reduce the error further. We conclude that even for low resolutions, high stiffness accuracy can be reached.

Next, we study the impact of the number of crystallites, i.e., the size of the volume element, which influences whether the volume element is representative. In Fig. 14, the anisotropic and shear modulus errors decrease as the number of crystals increases. The initial mean deviation from isotropy is 0.4 %, which reduces to about 0.04 %. The shear modulus error is lower than the deviation from isotropy for every considered set of parameters. It decreases significantly until it reaches a value of about 0.4 % at roughly 2048 crystallites, after which a further decrease cannot be conclusively observed. For both error values, the effect of increasing the number of crystallites appears greater than the effect of increasing the resolution.

After investigating the resolution dependence of the isotropic state, we turn our attention to textured polycrystals. We seek to quantify the influence of higher-order texture tensors on the effective stiffness for the copper example microstructure. To do so, we prescribe all texture tensors up to a given order, and compute the relative stiffness error as in (4.13), where the ground truth stiffness $\mathbb{C}$ computes as the statistical average of the effective stiffnesses of the 100 realizations with fully prescribed texture tensors. Simulation results with 8192 crystallites and 256 voxels per crystallite are visualized in Fig. 15. The microstructures without any prescribed texture coefficients, which do not take texture into account at all, show a sizable stiffness error of roughly 1.35 %. The fourth-order texture shows a slightly increased mean error of roughly 0.034 % versus 0.026 % for all higher-order microstructures. In addition to the visualized mean errors, we also observe a discrepancy between the averaged stiffnesses for each order, which is also roughly 1.35 % for the zeroth-order results, 0.02 % for the fourth-order results, and negligible for the other orders. This suggests that neglecting texture coefficients of fourth and sixth order induces a systematic error, not only a random error. For the material under consideration, prescribing texture tensors of eighth and higher order does not lead to a measurable improvement in accuracy.

Note that there is an established hypothesis in homogenization theory of polycrystals that the effective stiffness tensor depends only on texture tensors of up to fourth-order for weakly anisotropic materials [39]. In light of our results, it appears that copper is not weakly anisotropic (see Huang et al. [89]). We note that the improvement in accuracy due to including the sixth-order texture coefficient is rather small, although the corresponding coefficient is large.

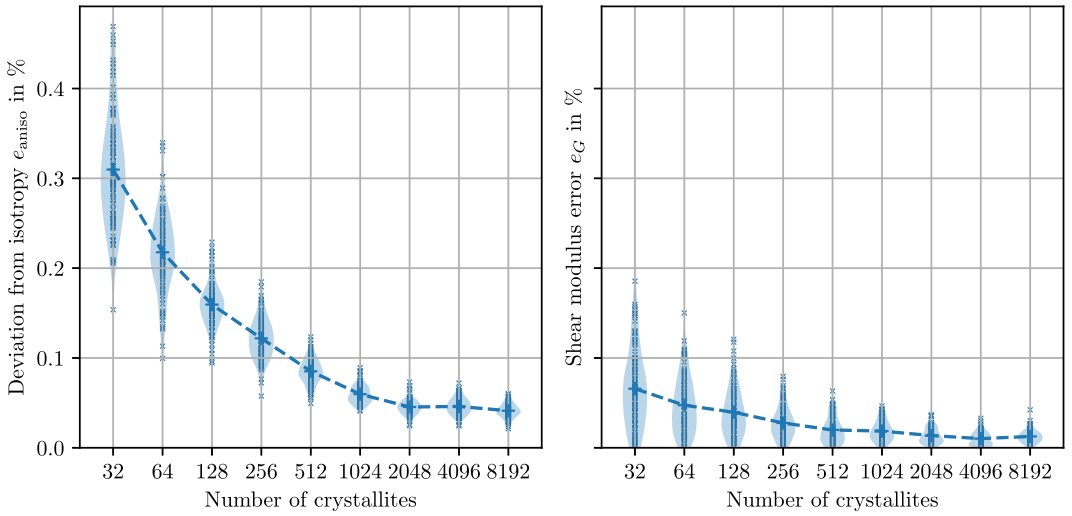

Fig. 14. Deviation from isotropy (left) and shear modulus error (right) for microstructures with varying numbers of crystallites resolved at 512 voxels per crystallite, with 100 realizations each. The reference shear modulus for the shear modulus error is obtained from one simulation with 16,384 crystallites using a resolution of 1024 voxels per crystallite.

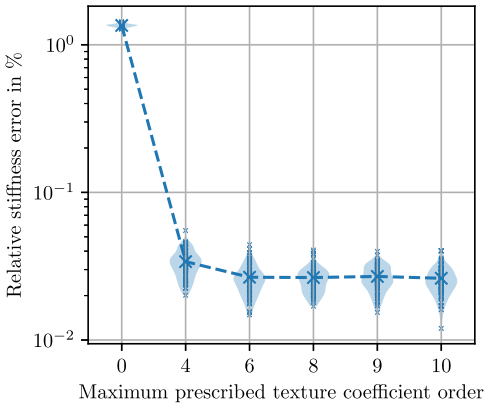

Fig. 15. Stiffness error for the copper example microstructure with prescribed texture tensors up to the given order. 100 simulations were performed for each order, with 8192 crystallites and 256 voxels per crystallite.

The Zener ratio [90]

$$Z = \frac{2\,C_{1212}}{C_{1111} - C_{1122}}. \tag{4.18}$$

for the elastic constants of copper given in Table 3 is roughly 2.21. Values far from unity indicate high anisotropy. To study the influence of the degree of anisotropy, we modify the Zener ratio, keeping the isotropic part of the single crystal stiffness, the moduli

$$K = C_{1111} + 2C_{1122}, \tag{4.19}$$

$$G = \frac{2}{5}\left(C_{1111} - C_{1122}\right) + \frac{6}{5}C_{1212}, \tag{4.20}$$

constant. The modified stiffness components compute as

$$C^*_{1111} = \frac{15\,G + 3\,KZ^* + 2\,K}{9(3Z^* + 2)}, \tag{4.21}$$

$$C^*_{1122} = \frac{-15\,G + 6\,KZ^* + 4\,K}{18(3Z^* + 2)}, \tag{4.22}$$

$$C^*_{1212} = \frac{5\,GZ^*}{4(3Z^* + 2)}. \tag{4.23}$$

Table 3
Material parameters for single-crystal elastoviscoplasticity simulations of copper [92].

Cubic stiffness	C_{1111} 170.2 GPa	C_{1122} 114.9 GPa	C_{1212} 61.0 GPa	
Flow rule	$\dot{\gamma}_0$ 0.001 s^{-1}	τ_0 6.5 MPa	τ_D 8 MPa	m 20
Hardening	θ_0 250 MPa	θ_∞ 14 MPa	τ_∞ 113.5 MPa	

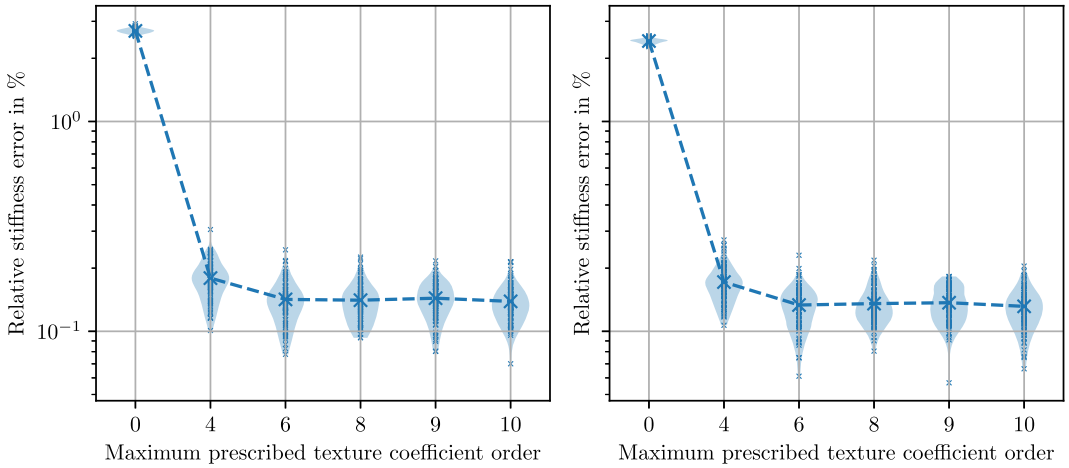

Fig. 16. Stiffness error for the example microstructure with modified Zener ratios $Z^* = 10$ (left) and $Z^* = 0.1$ (right) with prescribed texture tensors up to the given order. 100 simulations were performed for each order, with 8192 crystallites and 256 voxels per crystallite.

In Fig. 16, the stiffness error (4.13) is visualized for modified Zener ratios $Z^* = 10$ and $Z = 0.1$. These strongly anisotropic values serve as extremes of a range which covers most cubic materials, including the commonly encountered forms of elementary metals [91]. For either of the materials with modified Zener ratios, we find that the errors are significantly larger than for copper. However, the relative influence of the higher-order texture tensors remains the same. At extremely high anisotropy values, higher-order texture tensors might have a non-negligible influence on the stiffness. In the range of anisotropy investigated above, no higher-order influence is evident. We conclude that using texture tensors up to order six suffices for linear elastic homogenization of commonly encountered cubic materials.

4.4. Onset of plastic yield

The previous investigations confirmed that the influence of texture coefficients of order eight and above seems negligible for elasticity. In the section at hand, we investigate the related question for plastic properties of polycrystals. In particular, we investigate the transition between elastic and plastic regimes, i.e., plastic yielding.

Following experimental considerations, we define the yield stress R_{pX} as the stress in tensile direction reached in a uniaxial tensile test once the plastic strain in tensile direction – quantified by the equivalent von Mises plastic strain – reaches the value X. For plastically anisotropic materials, the yield stress R_{pX} depends on the tensile test direction $\boldsymbol{n}$. Having observed a clear dependence of the anisotropic stiffness on the texture coefficient of fourth order in Section 4.3, we wish to quantify the influence of the individual texture coefficients on the plastic response of an anisotropic polycrystal.

We investigate this question via numerical homogenization of centroidal Laguerre tessellations of copper. We model the material using crystal elastoviscoplasticity with a Chaboche overstress model for the viscoplastic flow rule (4.8), with a linear-exponential hardening curve

$$\tau_F = \tau_0 + (\tau_\infty - \tau_0)\left(1 - \exp\left(-\frac{\theta_0 - \theta_\infty}{\tau_\infty - \tau_0}\gamma\right)\right) + \theta_\infty \gamma, \tag{4.24}$$

where γ refers to the accumulated plastic slip over all N slip systems, with rate

$$\dot{\tau} = \sum_{k=1}^{N} |\dot{\gamma}_k|. \tag{4.25}$$

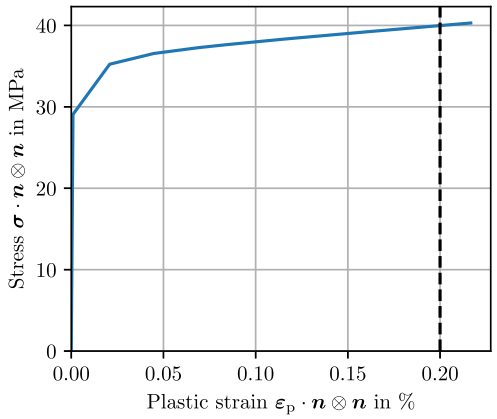

Fig. 17. Stress-plastic-strain-curve with $\varepsilon_p \cdot (n \otimes n) = 0.2\,\%$ marked as a dashed line.

We use the efficient numerical implementation of this material model by Wicht et al. [92]. Material parameters for copper are given in Table 3. As in the elastic computations, we discretize the voxelized microstructure on a staggered grid [87]. For the solver, we use a dual Newton-CG algorithm [93,94].

Given that our example material exhibits a rolling texture, we may imagine it as sheet metal. In this case, the yield stress anisotropy is of interest particularly in the sheet plane. Consequently, we perform tensile tests with a stress direction of

$$\boldsymbol{n} = \boldsymbol{R}_3(\omega)\boldsymbol{e}_1, \tag{4.26}$$

where $\boldsymbol{R}_3(\omega)$ is a rotation around the sheet normal axis $\boldsymbol{e}_3$ by an angle ω. For $\omega = 0°$, the loading direction is $\boldsymbol{e}_1$, while for $\omega = 90°$ it is $\boldsymbol{e}_2$. To compute the yield stress anisotropy, we perform tensile tests for each angle ω in 5° increments between those values. Each tensile test consists of ten loading steps up to a final effective strain of 0.25 %. In Fig. 17, the resulting macroscopic stress in load direction is plotted versus the plastic strain in load direction. For the small deformations under consideration, the hardening is well-approximated by a linear hardening rule with a constant hardening modulus of 250 MPa. The nonlinearity below 0.05 % plastic strain is related to the elastic-plastic transition, where an increasing number of crystallites plastify [95]. We linearly interpolate the obtain stress-plastic-strain curves to approximate the stress at a plastic strain of 0.2 %, i.e., $R_{p0.2}$. Given the above results, a lower threshold plastic strain would also be appropriate, such as 0.05 %. However, the value $R_{p0.2}$ is commonly reported from experiments. For brevity, we denote $R_{p0.2}$ as R.

We define the isotropic yield stress R_{iso} as the mean yield stress

$$R_{iso} = \frac{1}{2\pi} \int_0^{2\pi} R(\omega)\,\mathrm{d}\omega, \tag{4.27}$$

leaving an anisotropic remainder

$$R_{aniso}(\omega) = R(\omega) - R_{iso}. \tag{4.28}$$

We investigate the influence of the number of crystallites and voxels with a resolution study. As in the elastic case, the ground truth is an infinitely large polycrystal microstructure without prescribed texture tensors, leading to an isotropic orientation probability measure μ_{iso}. The anisotropic yield stress vanishes for the ground truth. As the isotropic yield stress is not known, we approximate it as the mean yield stress of the same reference microstructure as in the elastic case. We define the mean yield error

$$e^R_{iso} = R_{iso} - R^{ref}_{iso} \tag{4.29}$$

and the yield deviation from isotropy

$$e^R_{aniso} = \sqrt{\int_0^{2\pi} R_{aniso}(\omega)^2\,\mathrm{d}\omega}. \tag{4.30}$$

In Fig. 18, both errors are shown for microstructures with 8192 grains each and different resolutions. The yield deviation from isotropy is larger than the mean yield error in every case. As the number of voxels per crystallite increases, the means of both errors decreases. However, the trend is not particularly pronounced, suggesting that, even more so than in the elastic case, increasing the number of voxels per crystallite only brings small increases in accuracy.

We investigate the influence of the number of crystallites. Results with 512 voxels per crystallite and different numbers of crystallites are shown in Fig. 19. As in the elastic simulations, the number of crystallites has a large influence on the observed yield deviation from isotropy, which reduces with increasing numbers of crystallites from roughly 3 % to roughly 0.2 %. The mean yield error is lower than the yield deviation from isotropy error for every realization, and appears to plateau beyond roughly 1024 crystallites, at a value of roughly 0.06 %.

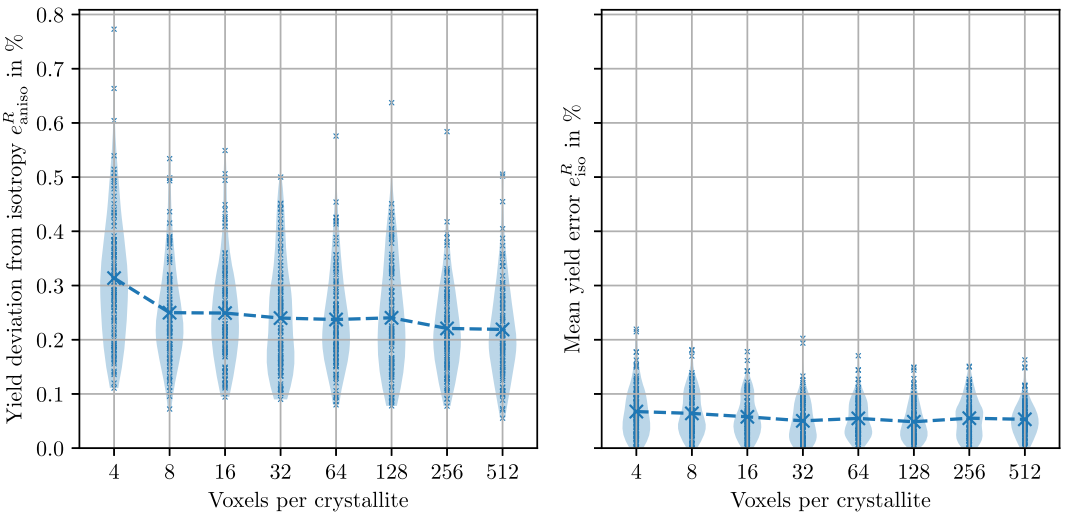

Fig. 18. Anisotropic (left) and isotropic (right) yield errors for microstructures with 8192 crystallites resolved using various numbers of voxels per crystallite, with ten realizations each. The reference isotropic yield stress for the isotropic errors was computed using one simulation with 16,384 crystals and a resolution of 1024 voxels per crystallite.

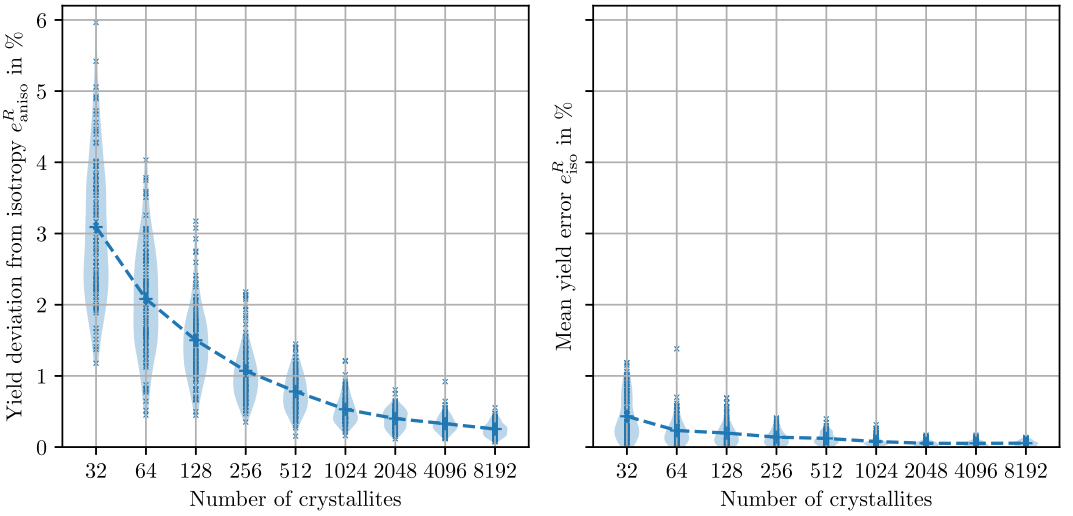

Fig. 19. Yield deviation from isotropy (left) and mean yield error (right) for microstructures with varying numbers of crystallites resolved at 512 voxels per crystallite, with 100 realizations each. The reference isotropic yield stress for the isotropic errors was computed using one simulation with 16,384 crystals and a resolution of 1024 voxels per crystallite.

In Fig. 20, the yield anisotropy is shown for different prescribed texture tensors. The shown yield values compute as the averaged yield stresses of 100 simulations each with 8162 crystallites and 256 voxels per crystallite. Unlike the stiffness anisotropy, the yield anisotropy is not well-approximated by prescribing only the fourth-order texture tensor. By including the sixth-order texture tensor, most relevant features of the yield surface appear to be incorporated. The tenth-order texture tensor is required to model a slight increase of the yield stress near the 30° angle.

In Fig. 21, yield errors are illustrated which compute as

$$e^R = \sqrt{\sum_{i=0}^{16} \left(R(\omega_i) - R(\omega_i)\right)^2}. \tag{4.31}$$

For the reference yield stiffness $R(\omega)$, the average of tenth-order results is used. The average error decreases monotonically with increasing prescribed texture order. This is unlike the linear elastic case, where no significant error reduction was observed for texture tensors higher than sixth order.

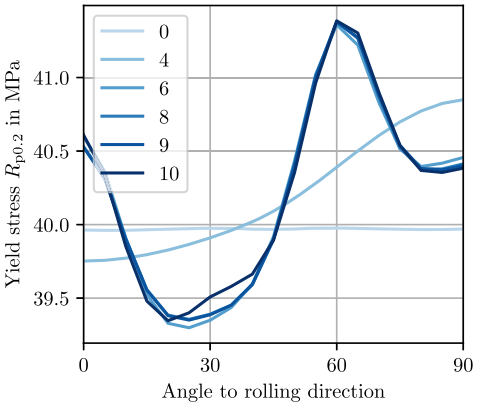

Fig. 20. Uniaxial tensile yield stress in different load directions for the copper example microstructure with prescribed texture tensors up to the given order.

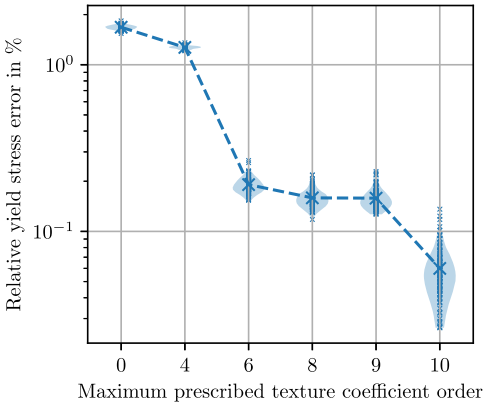

Fig. 21. Yield errors for the copper example microstructure with prescribed texture tensors up to the given order.

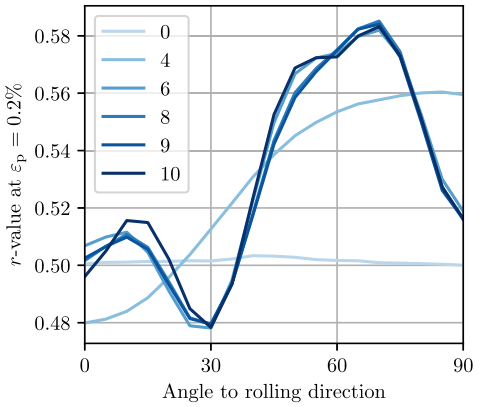

Fig. 22. r-values in different load directions for the copper example microstructure with prescribed texture tensors up to the given order.

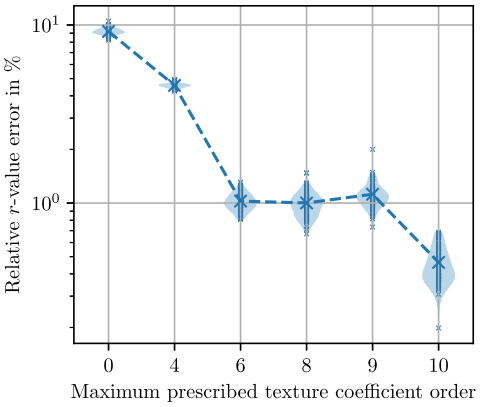

Fig. 23. Errors in the r-value for the copper example microstructure with prescribed texture tensors up to the given order.

In addition to anisotropic yield stresses, we investigate the r-value, a measure of plastic anisotropy commonly studied in sheet metal experiments and simulations. Following Hill [96], we define the r-value as the ratio

$$r = -\frac{\dot{\varepsilon}_{\mathrm{p}yy}}{\dot{\varepsilon}_{\mathrm{p}xx}}, \tag{4.32}$$

where $\dot{\varepsilon}_{\mathrm{p}xx}$ denotes the plastic strain rate component in load direction and $\dot{\varepsilon}_{\mathrm{p}yy}$ the same in sheet-plane direction orthogonal to the loading. The r-values are computed for same steps as the yield stress, i.e., as the x-component of the plastic strain reaches 0.2 %. The mean r-values computed over a hundred simulations – each with different prescribed texture orders – are shown in Fig. 22. As with the yield stress, including texture tensors up to order six appears sufficient to compute qualitatively accurate r-values, but for quantitative accuracy, including further texture tensors up to order ten is necessary.

In Fig. 23, errors in the r-values are illustrated, which compute as

$$e_{\mathrm{r}} = \sqrt{\sum_{i=0}^{16} \left(r(\omega_i) - r(\omega_i)\right)^2}. \tag{4.33}$$

in direct analogy to the yield stress error (4.31). A similar dependence on the texture error is observed as in Fig. 21 for the yield errors. However, the r-value errors are quantitatively larger, with up to 10 % error if texture is not taken into account at all.

We study the effect of single crystal elastic anisotropy by changing the Zener ratio (4.18), leading to modified stiffness components (4.21) as computed for the elastic simulations. Fig. 24 visualizes yield stress errors for Zener ratios of $Z^* = 10$ (left) and $Z^* = 0.1$ (right). Comparing the results with those for copper in Fig. 21, we find that the change of Zener ratio does not strongly affect the error. A minor change of the fourth-order influence for the low Zener ratio $Z^* = 0.1$ is observed. Otherwise, the results for different

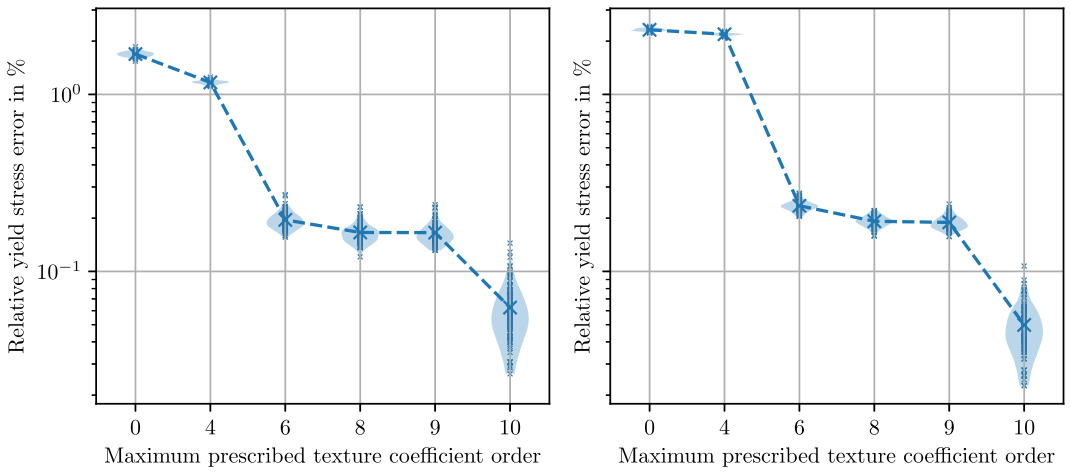

Fig. 24. Yield stress error for the example microstructure with modified Zener ratios $Z^* = 10$ (left) and $Z^* = 0.1$ (right) with prescribed texture tensors up to the given order. 100 simulations were performed for each order, with 8192 crystallites and 256 voxels per crystallite.

Zener ratios are indistinguishable. We conclude that the relative influence of the various texture orders of the onset of plastic yielding does not depend strongly on the degree of elastic anisotropy.

Based on our results, no general recommendation can be made to restrict texture tensors to less than tenth order. Consequently, efficient implementations of texture constraints on orientation sampling are critical to accurate microstructure generation.

5. Summary and conclusion

This work presents an algorithm for generating polycrystal microstructures with specified texture tensors. A special feature of this algorithm is the efficient performance for higher-order texture tensors, which allows us to investigate the influence of higher-order texture terms on effective properties of polycrystals computationally. We used the algorithm to investigate the anisotropy of stiffness and yield stress of rolled copper.

Prescribing texture tensors increases the accuracy of polycrystal simulations significantly. Notably, the microstructure generation procedure is significantly less computationally expensive than the homogenization procedure, making this accuracy improvement essentially free in terms of computational resources. As discussed in Section 2, prescribing texture coefficients is equivalent to a quadrature problem, suggesting a straightforward explanation for the increased accuracy: With properly chosen quadrature points, polynomials can be integrated exactly. Some aspects of computational homogenization involve integrals. Apparently, some of the involved functions are well-approximated by polynomials. As discussed in Appendix B, we did not manage to provide a proof that the quadrature problem with prescribed weights admits a solution with a finite number of crystallites. Our algorithm, as demonstrated in Section 4.2, is nonetheless capable of finding accurate computational solutions for this problem. Consequently, it may be possible to prove the existence of a solution with a finite lower bound on the number of crystallites. We note that in our approximate quadrature construction in Appendix B, we used the very general result of the Carathéodory theorem, which applies to any convex hull. Perhaps a proof using specific features of the problem at hand, such as the underlying rotation group $SO(3)$, is possible.

Matching texture coefficients in orientation sampling does not ensure that the generated microstructure is perfectly representative. As with any approach relying entirely on the ODF, a one-point statistic, spatial correlations between different grains are neglected. Correspondingly, we expect some remaining errors in the effective properties. Generally, we observe that the influence of low-order texture tensors is larger than that of higher-order texture tensors, where the rate at which the influence decreases depends on the material property which is being investigated. If texture tensors of sufficiently high order are taken into account, the non-texture error overshadows the error due to texture. While a texture model using only a finite number of coefficients may not be exact in the strict sense, it can still be sufficiently accurate that prescribing even higher coefficients brings no further improvements. For our example of rolled copper, we investigated these sufficient texture orders.

In linear elasticity, it appears that prescribing the fourth-order texture tensor takes care of the bulk of the texture-induced error. Indeed, many analytical homogenization approaches take only the fourth-order texture tensor into account [40]. We do however observe a further small influence of the sixth-order texture tensor, suggesting that the analytical approaches may be refined by including a sixth-order term. Prescribing texture tensors beyond order six brings no accuracy improvement in our simulation. The achieved stiffness error equals 0.026 %, which is already very small. We therefore conclude that prescribing texture tensors up to order six is sufficient for linear elastic homogenization of the material under consideration.

Studying the anisotropy of the macroscopic yield stress in the same material, we find that sixth-order texture tensors are not sufficient. Indeed, up to order ten, we observe a noticeable influence of prescribing further texture tensors not only on the value of the error, but also on the shape of yield anisotropy. Further studies are necessary to show whether the remaining error of roughly 0.6 %

can be further reduced by prescribing texture tensors of even higher order. We conclude that for nonlinear properties, prescribing higher-order texture tensors is crucial for accurate simulations.

The presented texture orientation optimization algorithm is not restricted to polycrystal microstructure generation methods based on tessellation models. More precisely, each polycrystal microstructure generation algorithm which assigns orientations in a post-processing step can be straightforwardly modified to use our orientation sampling algorithm.

As our orientation sampling algorithm takes only ODF-based statistics into account, it disregards higher-order correlation functions [12]. Deka et al. [19] propose an algorithm to incorporate misorientation statistics [18] of neighboring grains for microstructures with grains of equal size. Their algorithm re-assigns previously generated grain orientations as a post-processing step, making it compatible with our method. A more general approach to higher-order correlation may involve adding spatial correlation terms to the objective function of the orientation optimization problem. Either of these approaches seem viable for further study.

CRediT authorship contribution statement

Maximilian Krause: Writing – original draft, Visualization, Validation, Software, Methodology, Investigation, Formal analysis, Data curation, Conceptualization; **Thomas Böhlke:** Writing – review & editing, Supervision, Project administration, Methodology, Funding acquisition, Conceptualization; **Matti Schneider:** Writing – review & editing, Supervision, Software, Resources, Project administration, Methodology, Investigation, Funding acquisition, Conceptualization.

Data availability

The microstructure algorithm discussed in this manuscript is implemented in the open-source python package `crystallites` available at https://git.uni-due.de/publicsoftwareingmath/crystallites/. All microstructure data used in this study as well as the corresponding computational homogenization results are available on request.

Declaration of competing interest

The authors declare that they have no known competing financial interests or personal relationships that could have appeared to influence the work reported in this paper.

Acknowledgments

We thank the anonymous reviewers for their valuable comments and suggestions which improved the manuscript. M. Schneider and M. Krause acknowledge support by the European Research Council within the Horizon Europe program project 101040238. Additionally, T. Böhlke and M. Krause acknowledge support by the German Research Foundation (DFG) as part of project 512640977, 'Evaluation of non-linear $\sin^2(\psi)$-distributions in residual stress analysis based on a scale-bridging mechanical modeling'.

Appendix A. Approximating arbitrary continuous functions on $SO(3)$ using polynomials

The goal of this section is to use the polynomials $\mathcal{P}_\infty$ (2.27) to approximate arbitrary continuous functions $g \in C^0(SO(3))$ on the group $SO(3)$ to arbitrary precision, i.e., to show that for any continuous function $g \in C^0(SO(3))$ and any margin of error $\delta > 0$, there is a polynomial p such that the estimate

$$|p(\boldsymbol{Q}) - g(\boldsymbol{Q})| \leq \delta \tag{A.1}$$

holds for any element $\boldsymbol{Q} \in SO(3)$. If this property holds, the polynomials are *dense* in the continuous functions $C^0(SO(3))$.

To establish that the polynomials are dense (A.1), we resort to the Stone-Weierstrass Theorem. As a subset of continuous functions $\mathcal{P}_\infty \subseteq C^0(SO(3))$, the polynomials on the topological space $SO(3)$ are dense provided the following two conditions are valid:

(A) The set $\mathcal{P}_\infty$ forms a subalgebra of the space $C^0(SO(3))$, i.e., the set $\mathcal{P}_\infty$ is closed under linear combinations and multiplication.
(B) The set $\mathcal{P}_\infty$ separates points, i.e., if for any two distinct orientations on the manifold $SO(3)$ there exists a polynomial which has different values for the two points.

Condition (A) results directly from the fact that the set of tensors of arbitrary order are closed under addition and multiplication. The sum of two polynomials p_1, p_2 is a polynomial by definition (2.26). Two arbitrary polynomials p_1 and p_2 with coefficient pairs $(\mathbb{A}_1^m, \mathbb{B}_1^m)$ and $(\mathbb{A}_2^n, \mathbb{B}_2^n)$ have the product

$$p_1(\boldsymbol{Q})\, p_2(\boldsymbol{Q}) = \left(\mathbb{A}_1^m \otimes \mathbb{A}_2^n\right) \cdot \left(\boldsymbol{Q} \star \left(\mathbb{B}_1^m \otimes \mathbb{B}_2^n\right)\right), \tag{A.2}$$

which is a polynomial by definition (2.26) because it is represented by the coefficient pair $(\mathbb{A}_1^m \otimes \mathbb{A}_2^n, \mathbb{B}_1^m \otimes \mathbb{B}_2^n)$. For polynomials given by sums of other polynomials, a similar result follows after evaluating the distributive law. The set of polynomials $\mathcal{P}_\infty$ is closed under addition and multiplication, therefore forming a subalgebra of the continuous functions $C^0(SO(3))$.

We establish the validity of condition (B) constructively. For a fixed orientation $\boldsymbol{Q}_1$, we consider the linear polynomial

$$p : SO(3) \to \mathbb{R}, \quad p(\boldsymbol{Q}) = \boldsymbol{Q}_1 \cdot \boldsymbol{Q}, \tag{A.3}$$

where $\cdot$ denotes the inner product on the space of second-order tensors $\mathbb{R}^{3\otimes 2}$, i.e., a full tensor contraction. Due to the Cauchy-Schwarz inequality,

$$p(\boldsymbol{Q}) = \boldsymbol{Q}_1 \cdot \boldsymbol{Q} \leq |\boldsymbol{Q}_1 \cdot \boldsymbol{Q}| \leq \|\boldsymbol{Q}_1\| \|\boldsymbol{Q}\|. \tag{A.4}$$

The Frobenius norm $\|\boldsymbol{Q}\|$ of an orthogonal 3×3 matrix is $\sqrt{3}$. Consequently, the upper bound

$$p(\boldsymbol{Q}) \leq 3, \tag{A.5}$$

holds, and the equality $p(\boldsymbol{Q}) = 3$ is satisfied under the condition $\boldsymbol{Q} = \boldsymbol{Q}_1$ only. Therefore, the polynomial p separates the orientation $\boldsymbol{Q}_1$ from any other orientation, and condition (B) follows. As both prerequisites (A) and (B) of the Stone-Weierstrass Theorem are satisfied, the polynomials are dense in the continuous functions $C^0(SO(3))$.

Appendix B. Existence of a solution to the quadrature problem

We consider the moment-matching problem introduced in Section 2.2, and discuss the existence of a solution. Without prescribed weights, we find an existence proof by adapting prior results for the related fiber orientation tensor realization problem. However, with prescribed weights, we find only an approximate solution using an excessively large amount of crystallites.

First, we show the existence of a solution for a simplified quadrature problem with non-prescribed weights. We use a similar approach to Bauer et al. [97], who investigated a related realizability problem for fiber orientation tensors. Formally stated, we wish to show that for a given Borel probability measure μ, there exists a set of m orientations $\boldsymbol{Q}_\beta \in SO(3)$ with associated weights $w_\beta \in [0, 1]$ such that

$$\sum_{\beta=1}^{m} w_\beta = 1, \tag{B.1}$$

$$\int_{SO(3)} p(\boldsymbol{Q}) \, \mathrm{d}\mu(\boldsymbol{Q}) = \sum_{\beta=1}^{m} w_\beta p(\boldsymbol{Q}_\beta) \quad \text{for all} \quad p \in \mathcal{P}_n, \tag{B.2}$$

where $\mathcal{P}_n$ denotes the set of nth order polynomials (2.26). In other words, we seek to approximate a given Borel measure μ by a convex combination of a finite number of Dirac measures $\delta_{\boldsymbol{Q}_\beta}$ in such a way that polynomial functions up to degree n are integrated exactly. Convex sums of Dirac measures are dense in the space of Borel probability measures with respect to the weak-$*$ topology, which is a classical result of functional analysis, e.g., as a direct consequence of the Krein-Milman theorem [98]. Analogously to the statement (A.1), this fact implies that for the measure μ, there is a sequence $\mu_{\delta,\ell}$, such that for every function $p \in C_0(SO(3))$, we have

$$\int_{SO(3)} p(\boldsymbol{Q}) \, \mathrm{d}\mu_{\delta,\ell}(\boldsymbol{Q}) \to \int_{SO(3)} p(\boldsymbol{Q}) \, \mathrm{d}\mu(\boldsymbol{Q}) \quad \text{as} \quad \ell \to \infty. \tag{B.3}$$

According to Eq. (2.22), each discrete measure $\mu_{\delta,\ell}$ is a convex combination of r_ℓ Dirac measures $\delta_{\boldsymbol{Q}_{\beta,\ell}}$ with associated weights $w_{\beta,\ell}$. Substituting the convex sum into Eq. (B.3) leads to

$$\sum_{\beta=1}^{r_\ell} w_{\beta,\ell} \, p(\boldsymbol{Q}_{\beta,\ell}) \to \int_{SO(3)} p(\boldsymbol{Q}) \, \mathrm{d}\mu(\boldsymbol{Q}) \quad \text{as} \quad \ell \to \infty. \tag{B.4}$$

The next step is to show that if we restrict the approximation to a finite-dimensional space of functions p, there is an upper bound to the number of Dirac measures r_l. We use the polynomials of up to nth order $\mathcal{P}_n$, which form a vector space of dimension

$$d = \sum_{i=0}^{n} (2i+1)^2 = \frac{1}{3}(1+n)(1+2n)(3+2n), \tag{B.5}$$

which follows explicitly as the sum of the number of independent coefficients of the texture tensors $\{\mathbb{T}^{2i} | i \leq n\}$, see (2.36). By choosing tensorial bases as discussed in Section 2.3, we identify basis polynomials $\{p_i | i \leq d\}$ which span the space of nth order polynomials $\mathcal{P}^n$. We require Eq. (B.3) to hold for precisely those basis polynomials and write

$$\sum_{\beta=1}^{r_\ell} w_{\beta,\ell} \, p_i(\boldsymbol{Q}_{\beta,\ell}) \to \int_{SO(3)} p_i(\boldsymbol{Q}) \, \mathrm{d}\mu(\boldsymbol{Q}) \quad \text{as} \quad \ell \to \infty \quad \text{for all} \quad i \in \{1, 2, \ldots, d\}. \tag{B.6}$$

We interpret the basis functions p_i as components of a vector-valued function $\boldsymbol{p} : SO(3) \to \mathbb{R}^d$. Consequently, the values $p_i(\boldsymbol{Q}_{\beta,\ell}) \in \mathbb{R}$ are components of a vector $\boldsymbol{p}_{\beta,\ell} \in \mathbb{R}^d$. Carathéodory's theorem [99] states that any element in the convex hull $\mathrm{Conv}(H)$ of a set $H \subset \mathbb{R}^d$ in a finite-dimensional space with dimension d can be represented by a convex combination of elements of a finite subset $I \subseteq H$ with at most $d+1$ elements. In our case, the set H_ℓ is given by the set of polynomial value tensors $\{\boldsymbol{p}_{\beta,\ell}\}$, containing r_ℓ elements. Since the left-hand side of Eq. (B.6) is an element of the convex hull $\mathrm{Conv}(H_\ell)$, we find that a convex combination of at most $d+1$ elements is needed to represent it. We write

$$\sum_{t \in I_\ell} w_t \boldsymbol{t} \to \int_{SO(3)} \boldsymbol{p}(\boldsymbol{Q}) \, \mathrm{d}\mu(\boldsymbol{Q}) \quad \text{as} \quad \ell \to \infty. \tag{B.7}$$

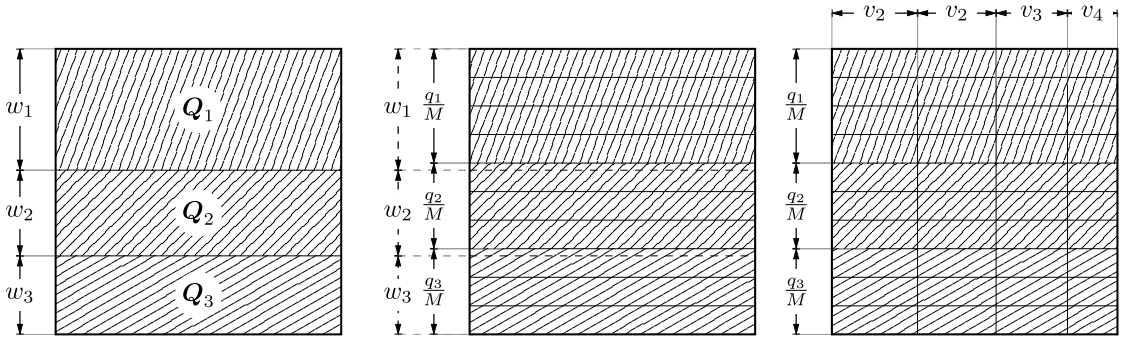

Fig. 25. Schematic illustration of three different quadrature approaches and their weights, with three orientations, a numerator $M = 10$ and $N = 4$ prescribed volume fractions.

The weight-value pairs $(w_t, \boldsymbol{t})$ are points in the product space $[0, 1] \times SO(3)$. Consequently, the discrete measure on the left-hand side of Eq. (B.7) is characterized by a point in the space $[0, 1]^{d+1} \times SO(3)^{d+1}$, which is compact. Being uniquely parametrized by a sequence in a compact space, the discrete measures contain a convergent subsequence. The limit of this subsequence as ℓ goes to infinity is again characterized by a point in the space $[0, 1]^{d+1} \times SO(3)^{d+1}$ and yields the exact integral

$$\sum_{t \in I} w_t \boldsymbol{t} = \int_{SO(3)} \boldsymbol{p}(\boldsymbol{Q}) \, \mathrm{d}\mu(\boldsymbol{Q}), \tag{B.8}$$

with $I \subset \mathbb{R}^d$ containing at most $d + 1$ elements. Thus, a finite number of quadrature points is sufficient to integratefactly.

However, this result holds only if the weights are not prescribed, whereas in our present case, the weights are given by volume fractions v_α. We could not find an existence proof for polynomially exact quadratures with prescribed weights in the literature. To begin with, we discuss the case of M equally-weighted quadrature points. From Eq. (B.8), we find a quadrature consisting of $d + 1$ weighted orientations. Each weight $w_\beta \in [0, 1]$ can be approximated to arbitrary precision by a rational number, i.e., for a given denominator $M \in \mathbb{N}$, there exists a numerator $q_\beta \in \mathbb{N}$ such that

$$\left| w_\beta - \frac{q_\beta}{M} \right| \leq \frac{1}{2N}. \tag{B.9}$$

For sufficiently large M, this approximation becomes arbitrarily precise. When approximating the set of weights $\{w_\beta\}$, we seek a set of numerators $\{q_\beta\}$ such that

$$\sum_{\beta=1}^{d+1} q_\beta = M \tag{B.10}$$

holds. In Fig. 25(b), this approximation is illustrated for three quadrature points and a denominator of $M = 10$.

The discussed technique for realizing equal volume fractions is readily modified to realize N prescribed volume fractions v_α. As illustrated in Fig. 25(c), we subdivide each of the $M = 10$ equal-volume crystallites into N sub-crystallites with volume fractions v_α / M. The final microstructure consists of MN crystallites and satisfies the prescribed crystallite sizes exactly, while satisfying the orientation statistics approximately, depending on the choice of the denominator M. This constructive example, while involving an excessive number of crystallites, illustrates the general feasibility of solving the moment-matching problem with prescribed volume fractions.

Appendix C. Symmetry properties of texture tensors

We discuss symmetry properties of the texture tensors introduced in Section 2.3. More precisely, we discuss the restrictions arising from material and statistical symmetries of a texture on its representation as a set of texture tensors. From these restrictions, we derive projector operators to compute symmetric texture tensors, allowing for efficient representation of symmetric textures.

Material symmetry requires that the crystal lattice is invariant under a subgroup of rotations

$$S \subseteq SO(3). \tag{C.1}$$

As the orientation statistics are meant to quantify the impact of lattice orientations on the material properties, only symmetry-invariant statistics are relevant. Therefore, we only need to consider polynomials respecting the invariance condition

$$p_i^m(\boldsymbol{Q}) = p_i^m(\boldsymbol{Q}\boldsymbol{R}) \quad \text{for all} \quad \boldsymbol{R} \in S. \tag{C.2}$$

Right-hand rotations apply to the texture tensors via

$$p^m(\boldsymbol{Q}\boldsymbol{R}) = \sum_{n=0}^{m} \frac{1}{2n+1} \mathbb{T}^{2n} \cdot \left(\boldsymbol{Q}^{\times n} \boldsymbol{R}^{\times n}\right), \tag{C.3}$$

$$= \sum_{n=0}^{m} \frac{1}{2n+1} \left(\mathbb{T}^{2n} \boldsymbol{R}^{\times n}\right) \cdot \boldsymbol{Q}^{\times n}, \tag{C.4}$$

where the multiplication between $2n$th order tensors is to be understood as a matrix-matrix multiplication between $(2n+1)\times(2n+1)$ matrices. Right-hand symmetry restricts the texture tensor $\mathbb{T}^{2n}$ to a right-hand symmetric subspace. As a tensor space, this subspace admits a right-hand basis consisting of tensors $\mathbb{D}^n_{S,i}$ which satisfy the symmetry condition

$$\boldsymbol{R} \star \mathbb{D}^n_{S,i} = \mathbb{D}^n_{S,i} \quad \text{for all} \quad \boldsymbol{R} \in S. \tag{C.5}$$

Depending on the symmetry class under consideration, the number of symmetric basis tensors $k_S(n)$ is significantly reduced compared to the full $(2n+1)$ degrees of freedom. The associated tensorial texture coefficients

$$\mathbb{V}^n_{S,i} = \int_{SO(3)} \boldsymbol{Q} \star \mathbb{D}^n_i \, \mathrm{d}\mu, \quad i \in \{1, 2, \dots, k_S(n)\} \tag{C.6}$$

are not generally S-symmetric. Using them, we write the symmetric texture tensor $\mathbb{T}^{2n}$ explicitly as

$$\mathbb{T}^{2n} = \sum_{i=1}^{k_S(n)} \mathbb{V}^n_{S,i} \otimes \mathbb{D}^n_{S,i}. \tag{C.7}$$

As an example, we consider the cubic lattice symmetry group, which is generated by 90° rotations around the three lattice vectors. A cubic set of deviatoric basis tensors up to order ten is listed in Appendix D. There are only five cubic basis tensors of up to order ten, whereas, in the fully anisotropic case, 120 basis tensors would be required in total.

Statistical symmetries of the texture correspond to left-hand symmetries of the texture tensors, which reduce the number of components of the coefficient tensor $\mathbb{V}^n$ just as the material symmetries reduce the number of deviatoric basis tensors $\mathbb{D}^n$. Of particular relevance is statistical isotropy, where the symmetry group S (C.1) equals the full group $SO(3)$. Because no deviatoric tensors of non-zero order are isotropic, statistical isotropy requires that all texture tensors of non-zero order vanish.

Appendix D. Cubic deviatoric basis tensors

The cubic deviatoric basis tensors are computed from the regular basis tensors by applying cubic symmetry, then re-orthonormalizing using the Gram-Schmidt procedure [100]. For texture tensors up order eleven, this procedure yields one tensor $\mathbb{D}^n_{\mathrm{C1}}$ per order $n \in \{0, 4, 6, 8, 9, 10\}$ As the results are ambiguous in their signs, we list the values we used explicitly for completeness:

$$D_{\mathrm{C1}} = 1, \tag{D.1}$$

$$\mathbb{D}_{\mathrm{C1}} = \frac{\sqrt{15}}{6}\mathbb{D}_1 + \frac{\sqrt{21}}{6}\mathbb{D}_9, \tag{D.2}$$

$$\mathbb{D}^6_{\mathrm{C1}} = -\frac{\sqrt{14}}{4}\mathbb{D}^6_5 + \frac{\sqrt{2}}{4}\mathbb{D}^6_{13}, \tag{D.3}$$

$$\mathbb{D}^8_{\mathrm{C1}} = \frac{\sqrt{195}}{24}\mathbb{D}^8_1 + \frac{\sqrt{21}}{12}\mathbb{D}^8_9 + \frac{\sqrt{33}}{8}\mathbb{D}^8_{17}, \tag{D.4}$$

$$\mathbb{D}^9_{\mathrm{C1}} = -\frac{\sqrt{42}}{12}\mathbb{D}^9_4 + \frac{\sqrt{102}}{12}\mathbb{D}^9_{12}, \tag{D.5}$$

$$\mathbb{D}^{10}_{\mathrm{C1}} = -\frac{\sqrt{1122}}{48}\mathbb{D}^{10}_5 - \frac{\sqrt{22}}{8}\mathbb{D}^{10}_{13} + \frac{\sqrt{390}}{48}\mathbb{D}^{10}_{21}. \tag{D.6}$$

References

[1] S. Torquato, Random Heterogeneous Materials, 16 of *Interdisciplinary Applied Mathematics*, Springer New York, New York, NY, 2002.
[2] S. Bargmann, B. Klusemann, J. Markmann, J.E. Schnabel, K. Schneider, C. Soyarslan, J. Wilmers, et al., Generation of 3D representative volume elements for heterogeneous materials: a review, Prog. Mater. Sci. 96 (2018) 322–384.
[3] T. Kanit, S. Forest, I. Galliet, V. Mounoury, D. Jeulin, et al., Determination of the size of the representative volume element for random composites: statistical and numerical approach, Int. J. Solids Struct. 40 (13) (2003) 3647–3679.
[4] M. Ostoja-Starzewski, Material spatial randomness: from statistical to representative volume element, Probab. Eng. Mech. 21 (2) (2006) 112–132.
[5] S. Mandal, J. Lao, S. Donegan, A.D. Rollett, et al., Generation of statistically representative synthetic three-Dimensional microstructures, Scr. Mater. 146 (2018) 128–132.
[6] P. Seibert, M. Husert, M.P. Wollner, K.A. Kalina, M. Kästner, et al., Fast reconstruction of microstructures with ellipsoidal inclusions using analytical descriptors, Computer-Aided Des. 166 (2024) 103635.
[7] S.G. Advani, C.L. III Tucker, The use of tensors to describe and predict fiber orientation in short fiber composites, J. Rheol. 31 (8) (1987) 751–784.
[8] M. Schneider, The sequential addition and migration method to generate representative volume elements for the homogenization of short fiber reinforced plastics, Comput. Mech. 59 (2) (2017) 247–263.
[9] A. Mehta, M. Schneider, A sequential addition and migration method for generating microstructures of short fibers with prescribed length distribution, Comput. Mech. 70 (4) (2022) 829–851.

[10] B. Chen, D. Li, P. Davies, R. Johnston, X. Ge, C. Li, et al., Recent progress of digital reconstruction in polycrystalline materials, Arch. Comput. Methods Eng. 32 (2025) 3447–3498.
[11] W.J. Boettinger, J.A. Warren, C. Beckermann, A. Karma, Phase-field simulation of solidification, Annu. Rev. Mater. Sci. 32 (2002) 163–194.
[12] M. Huang, The *N*-point orientation correlation function and its application, Int. J. Solids Struct. 42 (5) (2005) 1425–1441.
[13] D.T. Fullwood, S.R. Niezgoda, S.R. Kalidindi, et al., Microstructure reconstructions from 2-point statistics using phase-recovery algorithms, Acta Mater. 56 (5) (2008) 942–948.
[14] M.G. Rozman, M. Utz, Uniqueness of reconstruction of multiphase morphologies from two-point correlation functions, Phys. Rev. Lett. 89 (13) (2002) 135501.
[15] M. Fernández, F. Fritzen, On the generation of periodic discrete structures with identical two-point correlation, Proc. R. Soc. A 476 (2242) (2020) 20200568.
[16] C.L.Y. Yeong, S. Torquato, Reconstructing random media, Phys. Rev. E 57 (1) (1998) 495–506.
[17] P. Seibert, A. Raßloff, K. Kalina, M. Ambati, M. Kästner, et al., Microstructure characterization and reconstruction in python: MCRpy, Integr. Mater. Manuf. Innov. 11 (3) (2022) 450–466.
[18] C.L. Xie, S. Ghosh, M. Groeber, et al., Modeling cyclic deformation of HSLA steels using crystal plasticity, J. Eng. Mater. Technol. 126 (4) (2004) 339–352.
[19] D. Deka, D.S. Joseph, S. Ghosh, M.J. Mills, et al., Crystal plasticity modeling of deformation and creep in polycrystalline Ti-6242, Metall. Mater. Trans. A 37 (5) (2006) 1371–1388.
[20] F. Aurenhammer, F. Hoffmann, B. Aronov, et al., Minkowski-type theorems and least-squares clustering, Algorithmica (New York) 20 (1) (1998) 61–76.
[21] M. Groeber, S. Ghosh, M.D. Uchic, D.M. Dimiduk, et al., A framework for automated analysis and simulation of 3D polycrystalline microstructures. Part 2: synthetic structure generation, Acta Mater. 56 (6) (2008) 1274–1287.
[22] R. Quey, M. Kasemer, The neper/FEPX project: free / open-source polycrystal generation, deformation simulation, and post-processing, IOP Conf. Ser. 1249 (1) (2022) 012021.
[23] M.R.G. Prasad, N. Vajragupta, A. Hartmaier, et al., Kanapy: a python package for generating complex synthetic polycrystalline microstructures, J. Open Source Softw. 4 (43) (2019) 1732.
[24] M.A. Groeber, M.A. Jackson, DREAM.3D: A digital representation environment for the analysis of microstructure in 3D, Integr. Mater. Manuf. Innov. 3 (1) (2014) 56–72.
[25] P. Fernandez-Zelaia, J. Cheng, J. Mayeur, A.K. Ziabari, M.M. Kirka, et al., Digital polycrystalline microstructure generation using diffusion probabilistic models, Materialia 33 (2024) 101976.
[26] M. Buze, J. Feydy, S.M. Roper, K. Sedighiani, D.P. Bourne, et al., Anisotropic power diagrams for polycrystal modelling: efficient generation of curved grains via optimal transport, Comput. Mater. Sci 245 (2024) 113317.
[27] S.I. Wright, B.L. Adams, An evaluation of the single orientation method for texture determination in materials of moderate texture strength, Text., Stress, Microstruct. 12 (1–3) (1990) 359013.
[28] T. Baudin, J. Jura, R. Penelle, J. Pospiech, et al., Estimation of the minimum grain number for the orientation distribution function calculation from individual orientation measurements on Fe–3%Si and ti–4Al–6V alloys, J. Appl. Crystallogr. 28 (5) (1995) 582–589.
[29] L.S. Tóth, P. Van Houtte, Discretization techniques for orientation distribution functions, Text., Stress, Microstruct. 19 (4) (1992) 972830.
[30] M.A. Melchior, L. Delannay, A texture discretization technique adapted to polycrystalline aggregates with non-uniform grain size, Comput. Mater. Sci. 37 (4) (2006) 557–564.
[31] A. Biswas, N. Vajragupta, R. Hielscher, A. Hartmaier, et al., Optimized reconstruction of the crystallographic orientation density function based on a reduced set of orientations, J. Appl. Crystallogr. 53 (1) (2020) 178–187.
[32] G. Wassermann, J. Grewen, Texturen Metallischer Werkstoffe, Springer-Verlag, Berlin, 1962.
[33] T. Böhlke, U.-U. Haus, V. Schulze, et al., Crystallographic texture approximation by quadratic programming, Acta Mater. 54 (5) (2006) 1359–1368.
[34] R.-J. Roe, Description of crystallite orientation in polycrystalline materials. III. General solution to pole figure inversion, J. Appl. Phys. 36 (6) (1965) 2024–2031.
[35] H.-J. Bunge, Texture analysis by orientation distribution functions (ODF-analvsis) / texturanalyse mit hilfe von orientierungsverteilungsfunktionen (ODF-analyse), Int. J. Mater. Res. 68 (9) (1977) 571–581.
[36] Q.-S. Zheng, Y.-b. Fu, Orientation distribution functions for microstructures of heterogeneous materials (II)—Crystal distribution functions and irreducible tensors restricted by various material symmetries, Appl. Math. Mech. 22 (8) (2001) 885–903.
[37] M. Guidi, B.L. Adams, E.T. Onat, et al., Tensorial representation of the orientation distribution function in cubic polycrystals, Text., Stress, Microstruct. 19 (3) (1992) 673639.
[38] C.-S. Man, W. Du, Recasting classical expansion of orientation distribution function as tensorial Fourier expansion, J. Elast. 155 (1) (2024) 109–131.
[39] C.-S. Man, On the constitutive equations of some weakly-textured materials, Arch. Ration. Mech. Anal. 143 (1) (1998) 77–103.
[40] M. Lobos Fernández, T. Böhlke, Representation of Hashin–Shtrikman bounds in terms of texture coefficients for arbitrarily anisotropic polycrystalline materials, J. Elast. 134 (1) (2019) 1–38.
[41] C.-S. Man, M. Huang, Identification of material parameters in yield functions and flow rules for weakly textured sheets of cubic metals, Int. J. Nonlinear Mech. 36 (3) (2001) 501–514.
[42] C.L. Xie, E. Nakamachi, The effect of crystallographic textures on the formability of high-strength steel sheets, J. Mater. Process. Technol. 122 (1) (2002) 104–111.
[43] V. Hasija, S. Ghosh, M.J. Mills, D.S. Joseph, et al., Deformation and creep modeling in polycrystalline Ti–6Al alloys, Acta Mater. 51 (15) (2003) 4533–4549.
[44] G. Kurz, U.D. Hanebeck, Stochastic sampling of the hyperspherical von Mises–Fisher distribution without rejection methods, in: 2015 Sensor Data Fusion: Trends, Solutions, Applications (SDF), 2015, pp. 1–6.
[45] S. Kang, H.-S. Oh, Novel sampling method for the von Mises–Fisher distribution, Stat. Comput. 34 (3) (2024) 106.
[46] T. Leffers, D.J. Jensen, Evaluation of the effect of initial texture on the development of deformation texture, Text., Stress, Microstruct. 6 (4) (1986) 353901.
[47] P. Eisenlohr, F. Roters, Selecting a set of discrete orientations for accurate texture reconstruction, Comput. Mater. Sci. 42 (4) (2008) 670–678.
[48] R. Quey, A. Villani, C. Maurice, et al., Nearly uniform sampling of crystal orientations, Appl. Crystallogr. 51 (4) (2018) 1162–1173.
[49] A. Vuppala, A. Krämer, J. Lohmar, et al., On sampling discrete orientations from XRD for texture representation in aggregates with varying grain size, Crystals 11 (9) (2021) 1021.
[50] W. Liu, J. Lian, N. Aravas, S. Münstermann, et al., A strategy for synthetic microstructure generation and crystal plasticity parameter calibration of fine-grain-structured dual-phase steel, Int. J. Plast. 126 (2020) 102614.
[51] J. Kuhn, M. Schneider, P. Sonnweber-Ribic, T. Böhlke, et al., Generating polycrystalline microstructures with prescribed tensorial texture coefficients, Comput. Mech. 70 (3) (2022) 639–659.
[52] R.A. Lebensohn, C.N. Tomé, A self-consistent anisotropic approach for the simulation of plastic deformation and texture development of polycrystals: application to zirconium alloys, Acta Metall. Mater. 41 (9) (1993) 2611–2624.
[53] P.A. Turner, C.N. Tomé, A study of residual stresses in zircaloy-2 with rod texture, Acta Metall. Mater. 42 (12) (1994) 4143–4153.
[54] U.F. Kocks, J.S. Kallend, A.C. Biondo, et al., Accurate Representations of General Textures by a Set of Weighted Grains, Technical Report LA-UR-90-2828; CONF-9009236–1, Los Alamos National Lab., NM (USA), 1989.
[55] A. Eghtesad, T.J. Barrett, M. Knezevic, et al., Compact reconstruction of orientation distributions using generalized spherical harmonics to advance large-scale crystal plasticity modeling: verification using cubic, hexagonal, and orthorhombic polycrystals, Acta Mater. 155 (2018) 418–432.
[56] R.E. Marki, M. Knezevic, Nonlinear optimization for compact representation of orientation distributions based on generalized spherical harmonics, J. Mech. Phys. Solids 187 (2024) 105609.
[57] A. Bertram, T. Böhlke, N. Gaffke, B. Heiligers, R. Offinger, et al., On the generation of discrete isotropic orientation distributions for linear elastic cubic crystals, J. Elast. Phys. Sci. Solids 58 (3) (2000) 233–248.
[58] C.-S. Man, Crystallographic texture and group representations, J. Elast. 149 (1) (2022) 3–445.
[59] J. Barzilai, J.M. Borwein, Two-point step size gradient methods, IMA J. Numer. Anal. 8 (1) (1988) 141–148.

[60] Q.-S. Zheng, A.J.M. Spencer, On the canonical representations for kronecker powers of orthogonal tensors with application to material symmetry problems, Int. J. Eng. Sci. 31 (4) (1993) 617–635.
[61] V.V. Zhikov, S.M. Kozlov, O.A. Oleinik, et al., Homogenization of Differential Operators and Integral Functionals, Springer Berlin Heidelberg, Berlin, Heidelberg, 1994.
[62] H. Moulinec, P. Suquet, A fast numerical method for computing the linear and nonlinear mechanical properties of composites, C. R. Acad. Sci. Sé. II, Méc., Phys., Chim., Astron. 318 (11) (1994) 1417–1423.
[63] A. Bensoussan, J.-L. Lions, G. Papanicolaou, et al., Asymptotic Analysis for Periodic Structures, 374, North-Holland Publishing Company, Amsterdam, 1978.
[64] W.J. Drugan, J.R. Willis, A micromechanics-based nonlocal constitutive equation and estimates of representative volume element size for elastic composites, J. Mech. Phys. Solids 44 (4) (1996) 497–524.
[65] G.C. Papanicolaou, S.R.S. Varadhan, Boundary value problems with rapidly oscillating random coefficients, in: Random Fields, Vols. I, II, 27 of Colloq. Math. Soc., Janos Bolyai, Esztergom, 1979, pp. 853–873.
[66] N. Clozeau, M. Josien, F. Otto, Q. Xu, et al., Bias in the representative volume element method: periodize the ensemble instead of its realizations, Found. Comput. Math. 24 (4) (2024) 1305–1387.
[67] P. Etingof, B.L. Adams, Representations of polycrystalline microstructure by N-point correlation tensors, Text., Stress, Microstruct. 21 (1) (1993) 394321.
[68] S. Kaplan, On the second dual of the space of continuous functions, Trans. Am. Math. Soc. 86 (1) (1957) 70–90. 1992866
[69] R. Hill, Elastic properties of reinforced solids: some theoretical principles, J. Mech. Phys. Solids 11 (5) (1963) 357–372.
[70] I.M. Gelfand, R.A. Minlos, Z.Y. Shapiro, Representations of the Rotation and Lorentz Groups and Their Applications, Courier Dover Publications, 2018.
[71] M. Krause, T. Böhlke, Tensorial harmonic bases of arbitrary order with applications in elasticity, elastoviscoplasticity and texture-based modeling, Math. Mech. Solids 30 (5) (2024) 1188–1212.
[72] D.P. Bourne, S.M. Roper, Centroidal power diagrams, lloyd's algorithm, and applications to optimal location problems, SIAM J. Numer. Anal. 53 (6) (2015) 2545–2569.
[73] I.M. Sobol, Uniformly distributed sequences with an additional uniform property, USSR Comput. Math. Math. Phys. 16 (5) (1976) 236–242.
[74] J. Kuhn, M. Schneider, P. Sonnweber-Ribic, T. Böhlke, et al., Fast methods for computing centroidal laguerre tessellations for prescribed volume fractions with applications to microstructure generation of polycrystalline materials, Comput. Methods Appl. Mech. Eng. 369 (2020) 113175.
[75] S.W. Shepperd, Quaternion from rotation matrix, J. Guid. Control 1 (3) (1978) 223–224.
[76] M.E. Muller, A note on a method for generating points uniformly on *n*-Dimensional spheres, Commun. ACM 2 (4) (1959) 19–20.
[77] H. Dachsel, Fast and accurate determination of the wigner rotation matrices in the fast multipole method, J. Chem. Phys. 124 (14) (2006) 144115.
[78] S.T. Smith, Optimization techniques on riemannian manifolds, in: Hamiltonian and Gradient Flows, Algorithms and Control, 3 of *Fields Institute Communications*, Citeseer, 1994.
[79] C.J. Taylor, D.J. Kriegman, Minimization on the Lie Group SO (3) and Related Manifolds, Technical Report 9405, Yale University, 1994.
[80] A. Spettl, T. Werz, C.E. Krill, V. Schmidt, et al., Parametric representation of 3D grain ensembles in polycrystalline microstructures, J. Stat. Phys. 154 (4) (2014) 913–928.
[81] M. Krause, N. Simon, C. Klein, J. Gibmeier, T. Böhlke, et al.,(2025) Diffraction Stress Factors Calculated Using a Maximum Entropy Method (arXiv:2505.16370).
[82] G.I. Taylor, Plastic strain in metals, J. Inst. Met. 62 (1938) 307–324.
[83] T. Lin, Analysis of elastic and plastic strains of a face-centred cubic crystal, J. Mech. Phys. Solids 5 (2) (1957) 143–149.
[84] J. Lemaitre, J.-L. Chaboche, Mechanics of Solid Materials, Cambridge University Press, 1994.
[85] H.P. Klug, L.E. Alexander, X-Ray Diffraction Procedures: For Polycrystalline and Amorphous Materials, Wiley, Hoboken, 1974.
[86] T. Leffers, R.K. Ray, The brass-type texture and its deviation from the copper-type texture, Prog. Mater. Sci. 54 (3) (2009) 351–396.
[87] M. Schneider, F. Ospald, M. Kabel, et al., Computational homogenization of elasticity on a staggered grid, Int. J. Numer. Methods Eng. 105 (9) (2016) 693–720.
[88] J. Zeman, J. Vondřejc, J. Novák, I. Marek, et al., Accelerating a FFT-based solver for numerical homogenization of periodic media by conjugate gradients, J. Comput. Phys. 229 (21) (2010) 8065–8071.
[89] M. Huang, C.-S. Man, Constitutive relation of elastic polycrystal with quadratic texture dependence, J. Elast. 72 (1) (2003) 183–212.
[90] C. Zener, Contributions to the theory of beta-phase alloys, Phys. Rev. 71 (12) (1947) 846–851.
[91] S.I. Ranganathan, M. Ostoja-Starzewski, Universal elastic anisotropy index, Phys. Rev. Lett. 101 (5) (2008) 055504.
[92] D. Wicht, M. Schneider, T. Böhlke, et al., An efficient solution scheme for small-strain crystal-elasto-viscoplasticity in a dual framework, Comput. Methods Appl. Mech. Eng. 358 (2020) 112611.
[93] M. Kabel, T. Böhlke, M. Schneider, et al., Efficient fixed point and Newton–Krylov solvers for FFT-based homogenization of elasticity at large deformations, Comput. Mech. 54 (6) (2014) 1497–1514.
[94] L. Gélébart, R. Mondon-Cancel, Non-linear extension of FFT-based methods accelerated by conjugate gradients to evaluate the mechanical behavior of composite materials, Comput. Mater. Sci. 77 (2013) 430–439.
[95] F. Gehrig, D. Wicht, M. Krause, T. Böhlke, et al., FFT-based investigation of the shear stress distribution in face-centered cubic polycrystals, Int. J. Plast. 157 (2022) 103369.
[96] R. Hill, A theory of the yielding and plastic flow of anisotropic metals, Proc. R. Soc. Lond. Ser. A. Math. Phys. Sci. 193 (1033) (1948) 281–297.
[97] J.K. Bauer, M. Schneider, T. Böhlke, et al., On the phase space of fourth-order fiber-orientation tensors, J. Elast. 153 (2) (2023) 161–184.
[98] B. Simon, Extreme points and the krein–milman theorem, in: Convexity: an Analytic Viewpoint, number 187 in Cambridge Tracts in Mathematics, Cambridge University Press, Cambridge, 2011, pp. 120–135.
[99] C. Carathéodory, Über den variabilitätsbereich der Fourier'schen konstanten von positiven harmonischen funktionen, Rend. Circ. Mat. Palermo (1884–1940) 32 (1) (1911) 193–217.
[100] E. Schmidt, Zur theorie der linearen und nichtlinearen integralgleichungen, Math. Ann. 63 (4) (1907) 433–476.